

The JUICE 2024 close flyby of the Moon: Thermal assessment from MAJIS

Federico Tosi¹, Clément Royer², Federico Colaiuta^{3,1}, François Poulet², Tyler M. Powell⁴, Benjamin T. Greenhagen⁴, Yves Langevin², Alessandro Mura¹, Giuseppe Piccioni¹, Cédric Pilorget², Cristian Carli¹,
5 Francesca Zambon¹

¹Istituto Nazionale di Astrofisica – Istituto di Astrofisica e Planetologia Spaziali (INAF–IAPS), Rome, Italy

²Institut d’Astrophysique Spatiale, CNRS/Paris-Saclay University, Paris, France

³University of Rome “La Sapienza”, Department of Physics, Rome, Italy

⁴Johns Hopkins University – Applied Physics Laboratory (JHU–APL), Laurel (MD), USA

10 *Correspondence to:* Federico Tosi (federico.tosi@inaf.it)

Abstract. We present an analysis of four mid-infrared observations of the lunar surface acquired by the MAJIS instrument during the Jupiter Icy Moons Explorer (JUICE) gravity assist in August 2024. The data span 0.49–5.56 μm at sub-kilometre spatial resolution. These data provide a rare opportunity to investigate the challenging spectral regime where reflected solar radiation and thermal emission both contribute to the measured radiance.

15 The study explores three independent approaches to model and retrieve surface temperature and emissivity: (i) a Bayesian inversion framework, (ii) an empirical thermal correction method, and (iii) a roughness-informed thermophysical model. Rather than constituting a formal instrument validation, this paper provides a methodological consistency assessment of thermal retrieval strategies when applied to MAJIS mid-infrared data.

20 Retrieved temperature distributions are compared with expectations from established lunar thermal behaviour, and emissivity spectra are analysed in relation to known compositional contrasts between mare and highland terrains. The analysis highlights the sensitivity of the 3–5 μm crossover regime to modelling assumptions, temperature–emissivity coupling, and surface roughness parameterization.

25 Overall, the results demonstrate that MAJIS mid-infrared observations can be interpreted within physically consistent thermal modelling frameworks, while also revealing limitations and degeneracies inherent to this wavelength range. This workflow is directly transferable to future MAJIS observations of Jovian moons in the reflected–thermal crossover regime.

~~During the August 2024 lunar flyby of the Jupiter Icy Moons Explorer (JUICE), the MAJIS imaging spectrometer acquired the first hyperspectral observations of the Moon extending up to 5.56 μm at sub-kilometre resolution. This dataset provides an unprecedented opportunity to investigate the near-infrared thermal emission of the lunar surface and to validate MAJIS capabilities in a well-characterized planetary environment. We derive surface temperature and spectral emissivity using three independent approaches: a Bayesian inversion constrained by radiative transfer, an empirical correction based on laboratory relationships for lunar soils, and a roughness-informed thermal model that explicitly accounts for surface geometry and~~

anisothermality. All methods reproduce the expected dependence of temperature on solar illumination, while their divergences at high incidence angles highlight the role of roughness and unresolved topography. The roughness-informed model achieves the closest agreement with thermophysical predictions, whereas the Bayesian and empirical approaches exhibit complementary strengths under different illumination regimes. Emissivity retrievals consistently reveal higher values in mare regions than in surrounding highlands, reflecting known compositional and textural contrasts, and show a wavelength-dependent inversion relative to longer wavelength Diviner measurements. These results establish a validated framework for MAJIS thermal analysis of airless bodies and provide a benchmark for its future application to the investigation of the Jovian satellites.

1 Introduction

The European Space Agency's Jupiter ICy moons Explorer (JUICE) mission (Grasset et al., 2013), launched in April 2023, executed a close lunar flyby in August 2024 as part of its interplanetary trajectory toward Jupiter. While JUICE is optimized for the exploration of Jupiter's icy satellites, this flyby provided a critical opportunity to assess the instrumental performance of the scientific payload within a well-characterized planetary environment. For the Moons and Jupiter Imaging Spectrometer (MAJIS) (Poulet et al., 2024), this flyby served a dual purpose: assessing the performance of MAJIS data products and demonstrating its capability to retrieve physical and compositional surface properties under known lunar conditions at sub-kilometre spatial resolution and with unprecedented spectral resolution (Poulet et al., this issue). The present work is not intended as a formal, instrument-level validation of MAJIS. Topics such as absolute radiometric and spectral calibration (and its post-launch evolution), geometric calibration and pointing performance, and instrument thermal behaviour relevant to dark-signal subtraction and operability are addressed in dedicated companion papers (Langevin et al., this issue; Guerlet et al., this issue; Seignovert et al., this issue; Poulet et al., this issue, respectively). Although the modelling will provide a check of the absolute calibration of the IR channel, our focus is here on assessing the physical consistency and methodological robustness of thermal retrieval approaches applied to MAJIS mid-infrared observations of a well-characterized planetary surface.

Characterizing the Moon's surface thermal environment has been a long-standing scientific objective. Early ground-based and Earth-orbital telescopic observations provided bulk thermal properties and large-scale diurnal trends. The Apollo program acquired the first in situ heat flow measurements (e.g., Apollo 15, 17) and direct surface temperature records (Keihm et al., 1973; Keihm and Langseth, 1975). However, high-resolution orbital thermal mapping of the Moon only became routine with the Diviner Lunar Radiometer Experiment aboard NASA's Lunar Reconnaissance Orbiter (LRO) (Paige et al., 2010). Since 2009, Diviner has delivered near-global, multi-annual coverage of lunar surface temperatures at ~ 200 m/pixel resolution across multiple local times, enabling detailed studies of thermal inertia, rock abundance, rock size-frequency distributions, and volatile stability in permanently shadowed regions. Despite this revolutionary dataset, a significant observational gap remains in the near-infrared range $3.0\text{--}5.5\ \mu\text{m}$, where reflected sunlight and thermal emission overlap and where emissivity-temperature coupling is strongest which captures the Wien tail of the thermal emission and provides sensitivity to surface

~~emissivity variations linked to regolith texture, roughness, and composition.~~ This interval thus complements the longer-wavelength coverage of Diviner, extending high-resolution thermal measurements into a spectral domain previously unexplored at global scales.

Prior to JUICE, the Moon had been observed by other imaging spectrometers, although none provided the combination of spatial resolution and spectral coverage needed for detailed thermal analysis. The Moon Mineralogy Mapper (M³) onboard Chandrayaan-1 (Pieters et al., 2009) achieved near-global mineralogical mapping with a typical spatial resolution of 140 m/pixel but was limited to wavelengths shorter than 3 μm . The Visible and Infrared Mapping Spectrometer (VIMS) aboard Cassini (Brown et al., 2004) observed the Moon during its Earth swing-by in August 1999, mainly for the purpose of calibration. While VIMS covered wavelengths up to 5.1 μm , the data acquired during the lunar flyby suffered from both very coarse spatial resolution (~ 192 km/px) and severe saturation above 3.7 μm (Bellucci et al., 2002), which together precluded their use for any meaningful thermal mapping. Likewise, the JIRAM spectro-imager onboard NASA's Juno spacecraft (Adriani et al., 2017) acquired images and spectra of the Moon during the Earth flyby that occurred in October 2013, but with ~~coarse limited~~ spatial resolution (52–55 km/pixel), which enabled thermal retrieval in the range 3.0–4.2 μm mostly for the purpose of validating the instrument performances (Adriani et al., 2016). ~~Recently,~~ The Imaging Infrared Spectrometer (IIRS) on board Chandrayaan-2 (Chowdhury et al., 2020) acquired hyperspectral data of the Moon in the 0.8–5.0 μm range at a spatial resolution of approximately 80 m/pixel, demonstrating its capability to retrieve lunar surface temperatures and emissivity in the 3.0–5.0 μm range at local scale (Verma et al., 2022; Ojha et al., 2024). ~~In addition, disk-resolved single-band mid-infrared observations of the Moon at 3.5–4.1 μm (effective wavelength ~ 3.8 μm) were recently acquired by the geostationary Gaofen-4 satellite, providing a global reference for lunar radiance in the reflected–thermal crossover regime (Wu et al., 2021). More recently, the Moon was also observed in the thermal infrared during Lucy's 2022 Earth gravity assist with the L'TES instrument operating in the 5.8–100 μm spectral range, primarily as an in-flight calibration and validation target, providing high–spectral-resolution TIR spectra that are consistent with Diviner constraints and Apollo soil laboratory measurements (Christensen et al., 2025).~~ MAJIS observations during the JUICE flyby provide a complementary dataset characterized by a distinct illumination geometry, with a ~~broader~~ spectral range extending from 0.49 to 5.56 μm , and a different instrumental heritage, allowing ~~an independent consistency assessment of thermal retrieval approaches for independent validation of retrieval methods~~ and offering new insights into the thermophysical properties of specific lunar regions under varying solar illumination.

On August 19, 2024, during the JUICE Lunar Gravity Assist (LGA), in the outbound leg of the flyby shortly after closest approach, MAJIS acquired four hyperspectral images of the lunar surface in the overall spectral range 0.49–5.56 μm . We tag these observations respectively: C1, C2, C3 and C4. Taken from altitudes of 874 to 2406 km over the surface, these datasets yielded average pixel scales between 0.13 and 0.36 km/pixel, providing exceptional sub-kilometre infrared coverage across varying incidence angles and local times (a detailed description of the MAJIS data and the flyby geometry is documented in Poulet et al., this issue). Table 1 summarizes key specifications of the MAJIS LGA data. In the C4 observation, the first 17 out

of 64 pixels along the slit (“*samples*”) are not usable because the observation was purposely commanded to illuminate only part of the slit to evaluate the magnitude of straylight; therefore, they are ignored in the subsequent thermal analysis.

Table 1. Main features of the four hyperspectral images acquired by MAJIS during the JUICE flyby of the Moon on August 19, 2024.

	C1	C2	C3	C4
Filename	20240819211816	20240819211923	20240819212141	20240819212402
Start time (UTC)	2024-08- 19T21:18:16	2024-08- 19T21:19:24	2024-08- 19T21:21:42	2024-08- 19T21:24:02
Stop time (UTC)	2024-08- 19T21:19:06	2024-08- 19T21:21:31	2024-08- 19T21:23:49	2024-08- 19T21:25:26
Size (samples × lines × bands)	400 × 99 × 1016	64 × 1274 × 1016	64 × 1269 × 1016	64 × 841 × 1016
Altitude over the surface (km)	873.95 – 942.45	971.52 – 1269.24	1286.80 – 1813.27	1791.97 – 2406.05
Pixel resolution (km)	0.131 – 0.141	0.146 – 0.190	0.193 – 0.272	0.269 – 0.361
Phase angle (deg)	88.5 – 91.9	89.9 – 90.5	89.9 – 90.5	88.4 – 88.9
Solar incidence angle (deg)	85.0 – 93.1	66.2 – 83.7	44.4 – 65.2	26.3 – 45.1
Emission angle (deg)	0.2 – 7.0	8.2 – 26.0	25.2 – 47.9	43.4 – 65.7
Local solar time (h)	17.6 – 18.2	16.4 – 17.6	15.0 – 16.3	13.7 – 15.0

The JUICE/MAJIS flyby data complement the legacy of Diviner in two key ways: (1) they achieve spatial resolution comparable to Diviner during a targeted campaign, and (2) they extend high-resolution coverage into the 3.0–5.56 μm infrared spectral domain, which is under-explored for the Moon. Unlike Diviner’s broadband and multispectral thermal infrared (TIR) channels, MAJIS provides hyperspectral coverage across the 2.28–5.56 μm range with an average ~ 7 -nm spectral resolution (Haffoud et al., 2024). This interval captures the Wien tail of thermal emission and may include weak overtone or combination features of silicate materials. The hyperspectral capability enables the simultaneous retrieval of brightness temperature and spectral emissivity with high fidelity. Such data reveal subtle variations diagnostic of surface properties including roughness, regolith grain size, porosity, and composition—parameters that are often difficult to disentangle using broadband measurements.

Making the most of this small but **novel unique** dataset, the primary scientific objectives of the MAJIS lunar observations are: (1) to map diurnal temperature variability at high spatial resolution, (2) to retrieve spectral emissivity longward of 3 μm , and (3) to assess thermophysical properties where constrained by observation geometry. While the single flyby precludes broad-scale thermal inertia mapping, the hyperspectral data enable targeted thermophysical insights at specific locations. Localized modelling—leveraging distinct observation geometries, known crater morphology, and predicted self-heating effects—allows quantification of surface roughness at sub-kilometre scales. Furthermore, spectral emissivity retrievals provide independent

120 constraints on regolith texture (grain size, packing) intrinsically linked to thermophysical behaviour. These point estimates offer valuable validation against Diviner regional trends and in situ data.

Although the present analysis focuses on lunar observations, its relevance to the JUICE main mission lies primarily at the methodological level. The 4.5–5.5 μm spectral region investigated here corresponds to the crossover domain where reflected solar radiation and thermal emission coexist. The stability of temperature–emissivity separation in this regime, as well as the sensitivity of the inversion to prior assumptions, are largely independent of the specific target body and instead governed by radiative transfer physics and signal-to-noise characteristics.

In the Jovian system, this crossover regime is expected to be particularly relevant for Callisto, where the subsolar temperature value is approximately 165 K (Tosi et al., 2024, and references therein), allowing thermal emission to become detectable toward the long-wavelength edge of the MAJIS range (5.0–5.56 μm) (Royer et al., 2025). Ganymede may present a weaker but still measurable thermal contribution under favourable conditions, whereas Europa will likely represent a reflection-dominated case. While the physical parameters (albedo, emissivity spectra, thermal inertia, and surface roughness) must be adapted to icy regoliths, the inversion architecture and thermophysical modelling framework tested here remain directly applicable.

~~These targeted results advance understanding of small-scale lunar surface processes while serving as a critical proving ground for MAJIS methodologies. Quantifying roughness and texture under known lunar conditions can help validate techniques for interpreting thermal data from Ganymede, Callisto, and Europa, where similar sunlit observations by MAJIS are planned. The flyby thus directly bridges lunar science and JUICE’s core exploration goals.~~

In the remainder of this paper, Section 2 presents the derivation of surface temperature and emissivity from MAJIS data using three independent approaches: (i) a Bayesian nonlinear inversion constrained by radiative transfer, (ii) an empirical thermal correction adapted from laboratory-based relationships, and (iii) a roughness-informed, physically consistent thermal model. Before intercomparing these methods, we introduce a cross-wavelength context by incorporating co-located LRO/Diviner observations to establish an external benchmark for both temperature and emissivity (subsection 2.4). We then evaluate the performance of the three approaches in terms of their ability to reproduce observed thermal behaviour and emissivity contrasts across different terrains (subsection 2.5). Finally, in Section 3 we synthesize these results in a broader scientific discussion, drawing conclusions on the thermophysical properties of the lunar surface and outlining the implications for future applications of MAJIS to airless bodies in the outer Solar System.

2 Derivation of surface temperature and emissivity from MAJIS data

2.1 Bayesian approach to nonlinear inversion

The Bayesian nonlinear inversion used for MAJIS temperature retrieval builds upon techniques previously validated across multiple planetary missions. The methodology was routinely used on data acquired by the Dawn/VIR imaging spectrometer, which achieved nearly global coverage at asteroid Vesta and dwarf planet Ceres, leveraging the nonlinear radiance-temperature

relationship to infer thermophysical properties while accommodating rapid rotational cycles (Tosi et al., 2014; Capria et al., 2014; Tosi et al., 2015; Tosi et al., 2018). The methodology’s adaptability was further demonstrated on infrared data acquired by Rosetta/VIRTIS at the asteroid Lutetia (Keihm et al., 2012) and especially at the nucleus of comet 67P/Churyumov–
 155 Gerasimenko, resolving self-heating phenomena within shadowed concavities and diurnal thermal gradients at 15 m/pixel resolution (Tosi et al., 2019). Most directly, a similar Bayesian workflow was applied to JIRAM data of the Moon acquired during the 2013 Earth flyby of Juno to derive temperatures validated against LRO/Diviner data (Adriani et al., 2016).

The details of the Bayesian approach to nonlinear inversion are explained in the Appendix A of Tosi et al. (2014). Briefly, this technique addresses the inherent challenge of solving for multiple unknowns—temperature and wavelength-dependent
 160 emissivity—from a limited set of spectral radiance measurements. For a retrieval involving N spectral channels, the state vector includes N emissivity values plus the surface temperature, for a total of $N + 1$ free parameters.

The method follows the classical maximum-a-posteriori (MAP) formulation of Rodgers (2000), solved iteratively using a Gauss–Newton scheme. The radiative transfer model is linearized around an initial a priori state, and the optimal solution is obtained by minimizing a quadratic cost function combining the spectral misfit and the prior constraints. The associated
 165 posterior covariance matrix—derived from the inverse of the approximate Hessian of the cost function—provides the formal uncertainties of the retrieved parameters. In our implementation, the observation error covariance matrix S_e is defined using the in-flight Noise Equivalent Spectral Radiance (NESR) of MAJIS. In the absence of a validated model for channel-to-channel noise correlations, S_e is assumed diagonal, with wavelength-dependent variances given by the squared NESR. The a priori covariance matrix S_a applies soft constraints on temperature (± 30 K) and on emissivity, enforcing physically plausible values
 170 ($\varepsilon \leq 1$) and spectral smoothness. Emissivity correlations between neighbouring spectral channels are represented through off-diagonal terms in S_a , modelled with a Gaussian correlation function: for spectral channels i and j at wavelengths λ_i and λ_j , we set:

$$\text{cov}(\varepsilon_i, \varepsilon_j) = \sigma_{\varepsilon_i} \cdot \sigma_{\varepsilon_j} \cdot e^{-\frac{(\lambda_i - \lambda_j)^2}{l^2}} \quad i, j = 1 \dots N \quad (1)$$

175 where σ_{ε_i} is the a priori standard deviation assigned to emissivity at channel i and l is the correlation length (chosen comparable to the spectral sampling, in our case 20 nm which is about three MAJIS-IR spectral channels). This regularization mitigates the intrinsic temperature–emissivity degeneracy, especially near the crossover region where reflected and emitted components are comparable, and stabilizes the emissivity solution while preserving physically plausible variability (Rodgers, 2000).

The physical basis of the approach lies in the radiance equation for airless bodies, where the measured spectrum combines
 180 reflected solar and thermally emitted radiation. At thermal equilibrium, Kirchhoff’s law states that the spectral directional emissivity equals the corresponding spectral directional absorptivity. For an opaque surface (negligible transmittance), this can be written as $\varepsilon_d(\lambda) = 1 - r_{\text{hd}}(\lambda)$, where r_{hd} is the hemispherical–directional spectral reflectance. In the Bayesian retrieval, emissivity is treated as a spectral (channel-by-channel) directional quantity; no bolometric Kirchhoff relation is assumed. ~~Kirchhoff’s law ($r = 1 - \varepsilon$) links reflectance to emissivity, but~~ However, the system remains underconstrained without

185 additional prior information. The inversion therefore begins with an estimate of surface temperature obtained from the
brightness temperature in the dominant thermal-emission region, assuming an initial constant emissivity. An important
refinement is the dynamic determination of the crossover wavelength—the point at which reflected and emitted radiation are
equal—based on this temperature estimate. The spectral domain used in the inversion is then defined as extending from 0.5
190 μm shortward of this crossover to the long-wavelength limit of MAJIS sensitivity, ensuring that the crossover region is always
included for a stable emissivity solution.

Priors constrain the physically meaningful variability of the unknowns (± 30 K for temperature, and wavelength-dependent
bounds on emissivity to ensure $\varepsilon \leq 1$ and avoid nonphysical solutions). In practice, these values represent soft constraints: they
define the width of the a priori covariance matrix but do not impose hard limits. The Gauss–Newton iterations may therefore
converge outside these ranges if supported by the radiance data. Only two hard constraints are applied. First, emissivity values
195 exceeding unity are clipped to $\varepsilon = 1$. ~~Second, spectral segments are discarded when the Bayesian emissivity differs from the
Kirchhoff derived estimate by more than 4%, a criterion that removes artifacts near the crossover region.~~ Second, spectral
segments are discarded when the retrieved emissivity is inconsistent with Kirchhoff’s law by more than 4%, i.e. when
 $r(\lambda) = 1 - \varepsilon(\lambda)$ indicates non-physical behaviour near the crossover region. These steps prevent non-physical behaviour while
preserving the flexibility inherent in the Bayesian formulation. Formal uncertainties of temperature and emissivity are
200 computed from the posterior covariance and incorporate the in-flight ~~Noise Equivalent Spectral Radiance (NESR)~~, which
increases toward longer wavelengths due to spectrometer background.

A Bayesian formulation offers significant advantages over a simple least-squares fit when estimating temperatures from
infrared spectra, particularly when the available wavelengths lie in the Wien tail of the Planck function. In this regime, radiance
depends exponentially on temperature, creating a strong degeneracy between temperature and emissivity and making least-
205 squares solutions highly sensitive to noise and to the choice of initial emissivity. ~~In the present framework, this degeneracy is
regularized through the covariance structure imposed on the emissivity spectrum, which enforces smoothness across adjacent
wavelengths while allowing physically plausible variability. Although the Gauss–Newton implementation retrieves only the
local posterior maximum rather than the full posterior distribution, the posterior covariance naturally provides formal
uncertainties that reflect the structure of the inverse problem. By suppressing unrealistic high-frequency oscillations—
210 especially near the reflected/thermal crossover—the covariance-based regularization stabilizes the solution without imposing
mineralogical assumptions.~~

Compared to approaches that fit a Planck function with a single emissivity value, the Bayesian retrieval therefore uses the
covariance-based prior to regularize the temperature–emissivity degeneracy in a physically motivated way. Tighter spectral
correlations suppress noise more efficiently but increase the risk of over-regularization, whereas looser correlations allow
215 greater variability at the expense of stability.

~~Instead of relying on a scalar emissivity fitted simultaneously with T , the MAP framework adopted here uses a full covariance
matrix of the unknowns to regularize this degeneracy. Although the Gauss–Newton implementation retrieves only the local
posterior maximum rather than the full posterior distribution, the posterior covariance naturally provides formal uncertainties~~

that reflect the structure of the inverse problem. In particular, spectral covariance imposes smoothness across adjacent
220 wavelengths—consistent with the behaviour of natural granular materials—while allowing physically plausible variability.
Compared to other methods that fit a Planck function with a single emissivity value, the Bayesian retrieval exploits the full
covariance matrix of the unknowns as a genuine a priori. This matrix encodes expectations about how emissivity varies with
wavelength, enforcing smoothness through statistical correlations between neighbouring spectral channels—here modelled
with Gaussian decay over a correlation length comparable to the spectral resolution. This suppresses high-frequency noise and
225 reflects the physical reality that natural surfaces lack abrupt spectral features. In regions where radiance data are ambiguous—
such as near the crossover between reflected sunlight and thermal emission—the covariance matrix stabilizes the solution,
preventing unrealistic oscillations. It also governs the formal uncertainties, balancing constraint and flexibility: tighter
correlations reduce noise but risk over-regularization, while looser ones capture more variability at the expense of stability.
The result is a spectral regularizer rooted in physical smoothness rather than mineralogical assumptions.

230 Subsequent iterations refine temperature and emissivity simultaneously. For each pixel, the algorithm iterates up to 50 times,
recalculating the Jacobian matrix (radiance sensitivity to parameter changes) at each step to update the solution and its
uncertainties. Post-retrieval validation removes emissivity data affected by saturation or inconsistent with the Bayesian
solution, ensuring robustness. The method achieves convergence even with suboptimal initial guesses, yielding reliable results
for temperatures >170 K (the exact limit depends on sensitivity range and instrument thermal conditions) for dayside
235 measurements. Typical formal uncertainties are 1–3 K for temperature in well lit areas and 0.01–0.20 for emissivity, increasing
for low-temperature and/or high incidence angle scenarios.

For MAJIS, the heritage methodology was systematically adapted to lunar conditions. First, we consider data acquired only in
the infrared (IR) channel, which covers the spectral range 2.28–5.56 μm . Raw data underwent reinsertion of the background
signal (which is automatically subtracted in the calibration pipeline) to identify saturation artifacts, which appear as plateaus
240 in the spectral profile, sometimes with oscillations. Spectral pixels (“*spectels*”) exceeding 10,400 Digital Numbers (DN)—a
threshold empirically derived from C4 data, which experience the highest solar illumination—were flagged and excluded.
Synthetic radiance spectra were generated by combining thermal emission with reflected solar components modelled using the
MODTRAN Cebula+Kurucz extraterrestrial solar spectrum (<https://www.nrel.gov/grid/solar-resource/spectra.html>) scaled for
the heliocentric distance of the Moon at the time of the observation (1.014 au). Several hypotheses on the initial emissivity
245 (0.70–0.95) were evaluated, and the initial temperature was set equal to the brightness temperature in the 5.27–5.56 μm range,
allowing both parameters to vary within noise constraints until convergence. Two spectral ranges were tested: the
computationally efficient 4.5–5.56 μm window (Table A1) and the broader 3.0–5.56 μm interval (Table A2), the latter reducing
saturation biases in high-temperature regions at the cost of increased processing load. **We treat this as a stability–information
trade-off: the wider range increases leverage but also amplifies calibration/reflectance sensitivities in the crossover domain.**
250 The Lommel–Seeliger disk function (Hapke, 1981)—a photometric law optimized for the Moon—was also tested to account
for illumination and viewing geometry (Table A3).

Geometric precision was ensured through SPICE kernel navigation data (Acton, 1996; Acton et al., 2018) and instrument kernels, defining ellipsoid-level planetocentric coordinates as well as solar incidence and emission angles. The LEGA observations enable an update of the MAJIS instrument kernel, with details provided in a companion paper dedicated to the geometric calibration (Seignovert et al., this issue). ~~Topographic effects may be mitigated using a digital shape model to compute local illumination and emission angles.~~ Topographic effects could in principle be mitigated using a digital elevation/shape model to compute local illumination and emission angles; however, no DEM-based topographic correction is applied in this work. ~~However, while such corrections are critical for irregularly shaped bodies such as asteroids and comets, as well as for high-resolution optical imagery in general, approximating the Moon's shape as a smooth ellipsoid is acceptable in the case of MAJIS data, whose pixel scale is on the order of a few hundred meters.~~ While such corrections are critical for irregular bodies (e.g. asteroids and cometary nuclei), approximating the Moon as a smooth ellipsoid is adequate for the large-scale interpretation of MAJIS data at a spatial resolution of a few hundred metres per pixel. On the other hand, this approximation does not capture unresolved local slopes and shadowing, which may contribute to pixel-scale discrepancies. Emissivity outputs were restricted to the spectral range used for temperature retrieval (4.5–5.56 μm and 3.0–5.56 μm).

Using the range 4.5–5.56 μm , the temperature values obtained through the Bayesian inversion across the four MAJIS lunar observations (C1 to C4) reveal systematic dependencies on both the level of solar illumination and the choice of prior emissivity. As expected, the mean surface temperature increases from C1 through C4, reflecting progressively stronger solar heating (Figures 1–2). C1, acquired under grazing illumination, shows the lowest mean temperatures (~ 176 – 184 K), while C4, obtained under near-equatorial midday conditions, yields mean temperatures approaching 356–343 K, depending on the emissivity prior (Figure 3 and Table A1). ~~To quantify the dependence of the retrieval on the emissivity prior, we evaluate the spread of the retrieved mean temperatures obtained using $\epsilon_0 = 0.70, 0.80, 0.90,$ and 0.95 (Table A1). For the 4.5–5.56 μm retrieval window, the mean temperature varies by $\Delta T_{\text{mean}} \approx 8.6$ K (C1), 2.2 K (C2), 9.2 K (C3), and 12.9 K (C4) across the tested priors. This confirms that the sensitivity to ϵ_0 is generally limited for intermediate illumination conditions (C2), whereas it becomes more significant under extreme thermal regimes, where the radiance–temperature relationship is strongly nonlinear and temperature–emissivity degeneracy is enhanced.~~

A representative example of the spectral fit and the associated posterior temperature distribution for ~~two specific MAJIS pixels (optimal and sub-optimal) an individual MAJIS pixel~~ is shown in Figure A1, illustrating the behaviour of the Bayesian inversion described above.

280

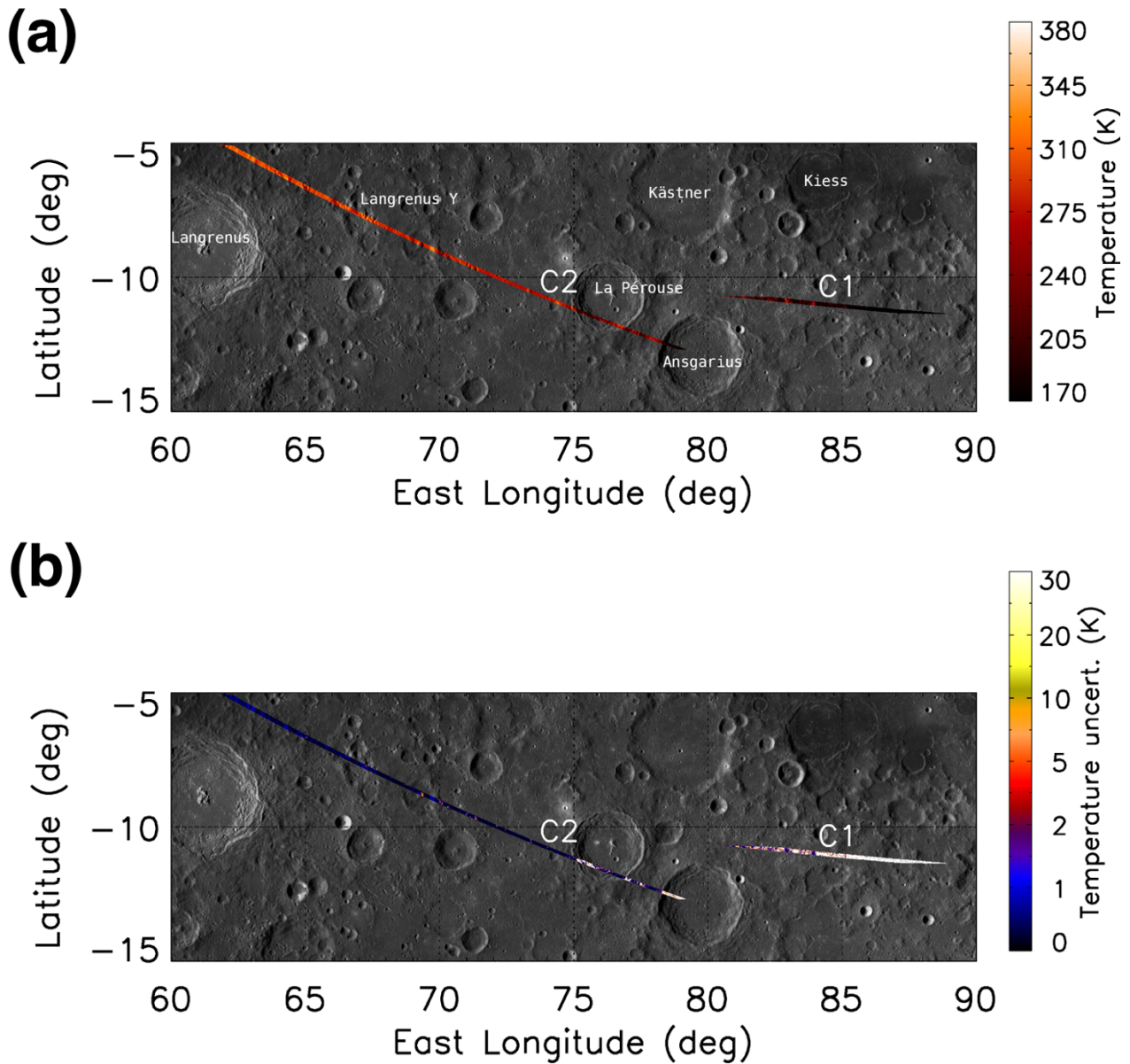
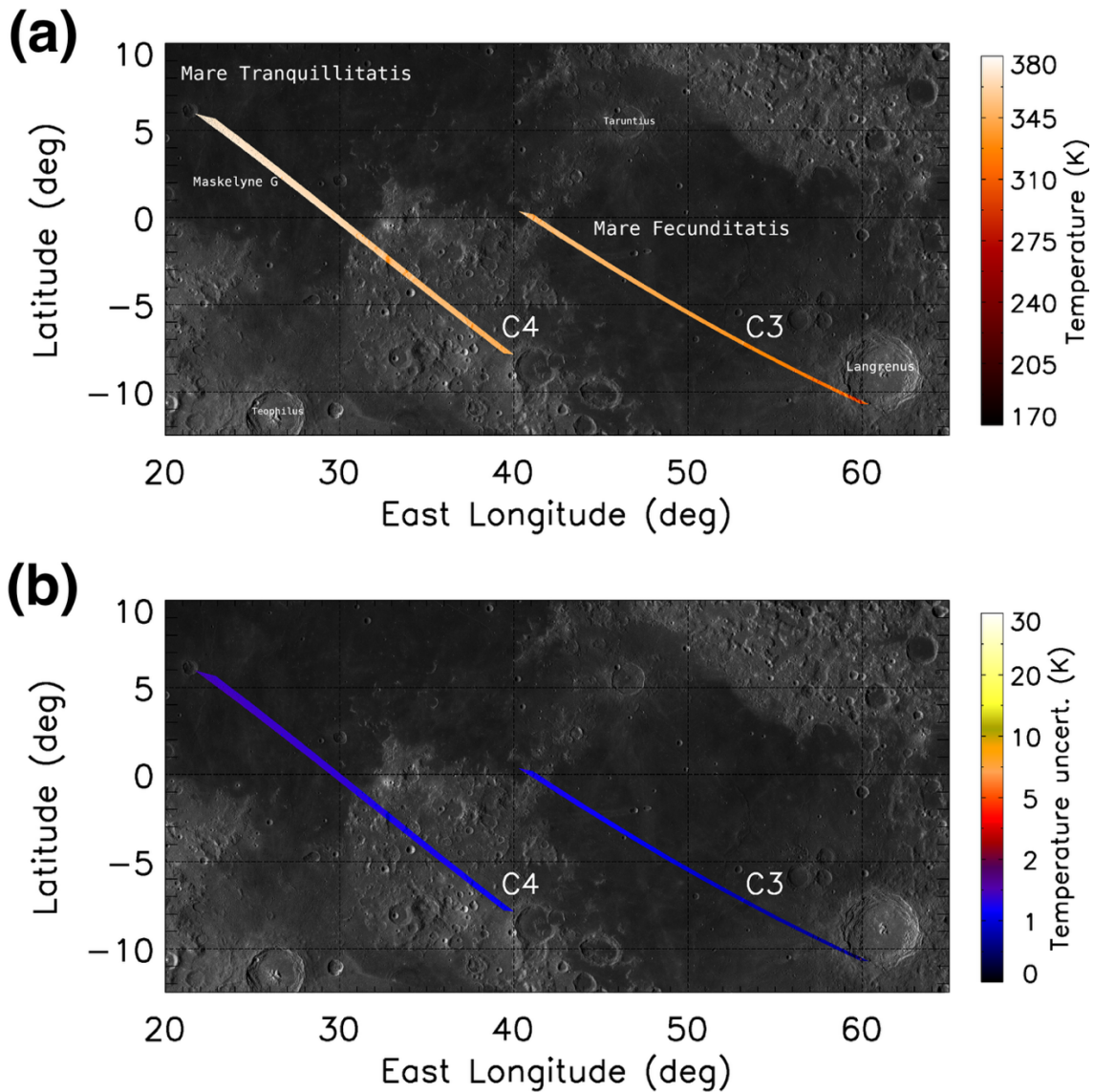
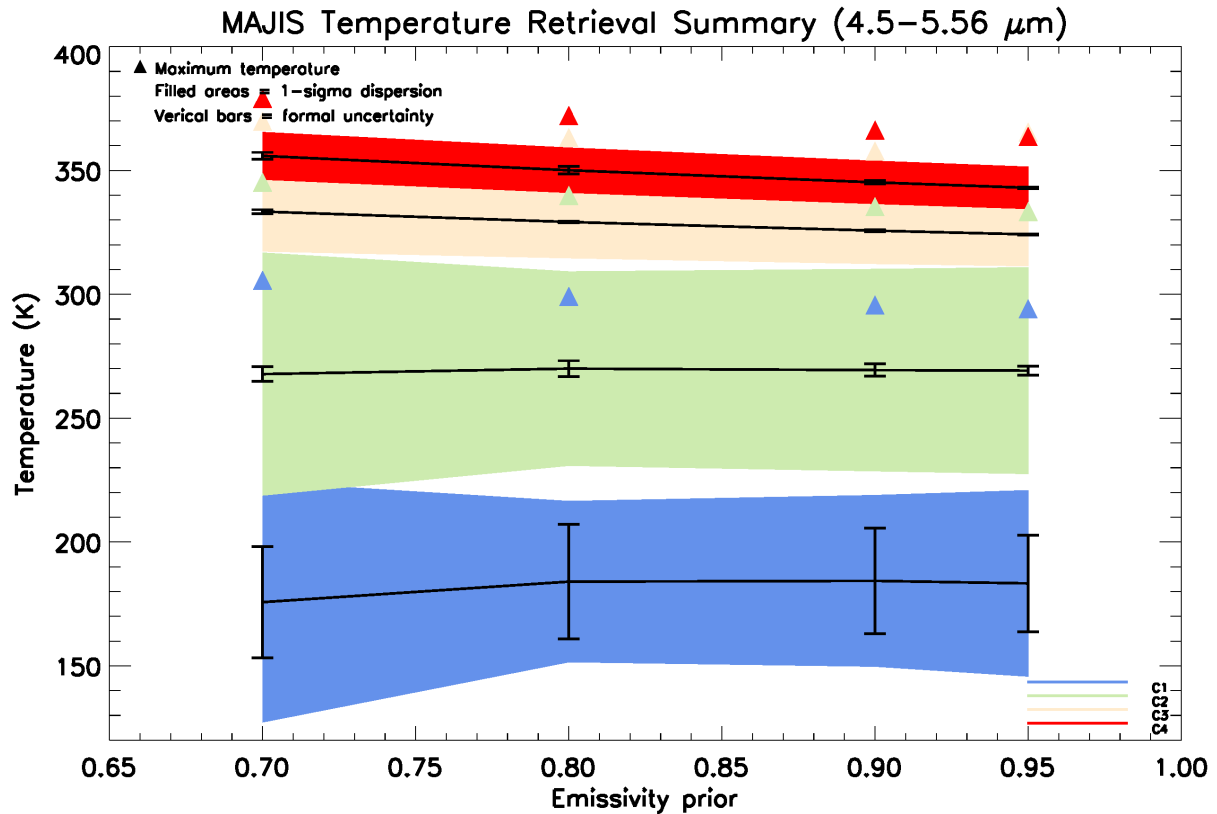


Figure 1. Bayesian temperature retrievals (C1–2). (a) Temperature maps derived from MAJIS observations C1 and C2, using the Bayesian approach applied to the 4.5–5.56 μm portion of the IR data using an emissivity prior of 0.70 ± 0.15 and no photometric correction. C1 is the easternmost data, taken near the terminator. C2 extends from northwest to southeast at low southern latitudes. Both data cover lunar highlands. Pixel resolution goes from 0.19 to 0.36 km. Colour gradation is mainly due to instantaneous solar illumination combined with local topography. (b) Formal uncertainties associated with the retrieved temperature values. The largest uncertainties are associated with the lowest temperature values, corresponding to unlit locations. Background image: Moon LRO LROC WAC Global Morphology Mosaic 100m, June 2013 (Speyerer et al., 2011; Wagner et al., 2015).



290 **Figure 2. Bayesian temperature retrievals (C3–4).** (a) Temperature maps derived from MAJIS observations C3 and C4, using the Bayesian
 approach applied to the 4.5–5.56 μm portion of the IR data under an emissivity prior of 0.70 ± 0.15 and no photometric correction. C3 is the
 easternmost data and mostly covers Mare Fecunditatis, bordering Langrenus crater in the southeastern edge. C4 is the westernmost data and
 embraces Mare Tranquillitatis and highlands in between Tranquillitatis and Fecunditatis. Both data extend from northwest to southeast at
 low southern latitudes, crossing the equator. Pixel resolution goes from 0.13 to 0.19 km. The colour gradation reaches its maximum on the
 scale, about 380 K, at the westernmost points of C4, which experience early afternoon. (b) Formal uncertainties associated with the retrieved
 295 temperature values. Typical average uncertainty is ~ 1 K. Background image: Moon LRO LROC WAC Global Morphology Mosaic 100m,
 June 2013 (Speyerer et al., 2011; Wagner et al., 2015).



300 **Figure 3. Summary of MAJIS temperature retrievals as a function of emissivity prior (4.5–5.56 μm spectral range).** The coloured bands represent the retrieved mean surface temperature (solid lines) and the corresponding $\pm 1\sigma$ dispersion for the four MAJIS observations (C1–C4). Vertical black bars indicate the formal uncertainties associated with the Bayesian inversion, while triangles mark the maximum temperature values observed within each dataset. The results illustrate the sensitivity of the retrieved temperature to the assumed emissivity: for the warmer datasets (C3 and C4), the mean temperature decreases slightly with increasing emissivity prior, while for the colder, high incidence cases (C1 and C2) the dependence on the emissivity prior is weak and does not follow a strictly monotonic trend. Small, irregular variations with prior reflect low thermal signal, local illumination/topography and retrieval noise rather than a systematic physical response.

305

As expected, the choice of initial emissivity (ϵ_0) influences the retrieved temperatures. Lower assumed emissivity values yield higher temperature estimates, due to the inverse relationship between emissivity and brightness temperature in the Planck function. In high-SNR observations such as C4, this leads to differences in mean temperature as large as 13 K across the range of tested priors. In contrast, datasets acquired at higher incidence angles (e.g., C1 and C2) exhibit smaller temperature shifts across priors, likely because shadowed regions dominate the radiance signal, flattening the temperature distribution and dampening the sensitivity to ϵ_0 .

310

The uncertainties associated with the retrieved temperatures show a more pronounced dependence on both solar illumination and the width of the emissivity prior. Formal uncertainties and $1\text{-}\sigma$ dispersions are significantly higher in C1 and C2, particularly when using broad priors (e.g., $\varepsilon_0 = 0.70 \pm 0.15$), reflecting the limited thermal contrast and stronger model degeneracy under low radiance conditions. In contrast, observations with higher insolation—namely C3 and C4—yield markedly lower formal errors and temperature dispersion. This reduction in spread is not only a function of radiometric quality but also of scene illumination: in C4, the entire observed area is well lit, and the few remaining shadows are due solely to local topography. This homogeneity in thermal forcing minimizes temperature variability across the scene and enhances retrieval precision, reinforcing the robustness of the Bayesian approach under favourable conditions.

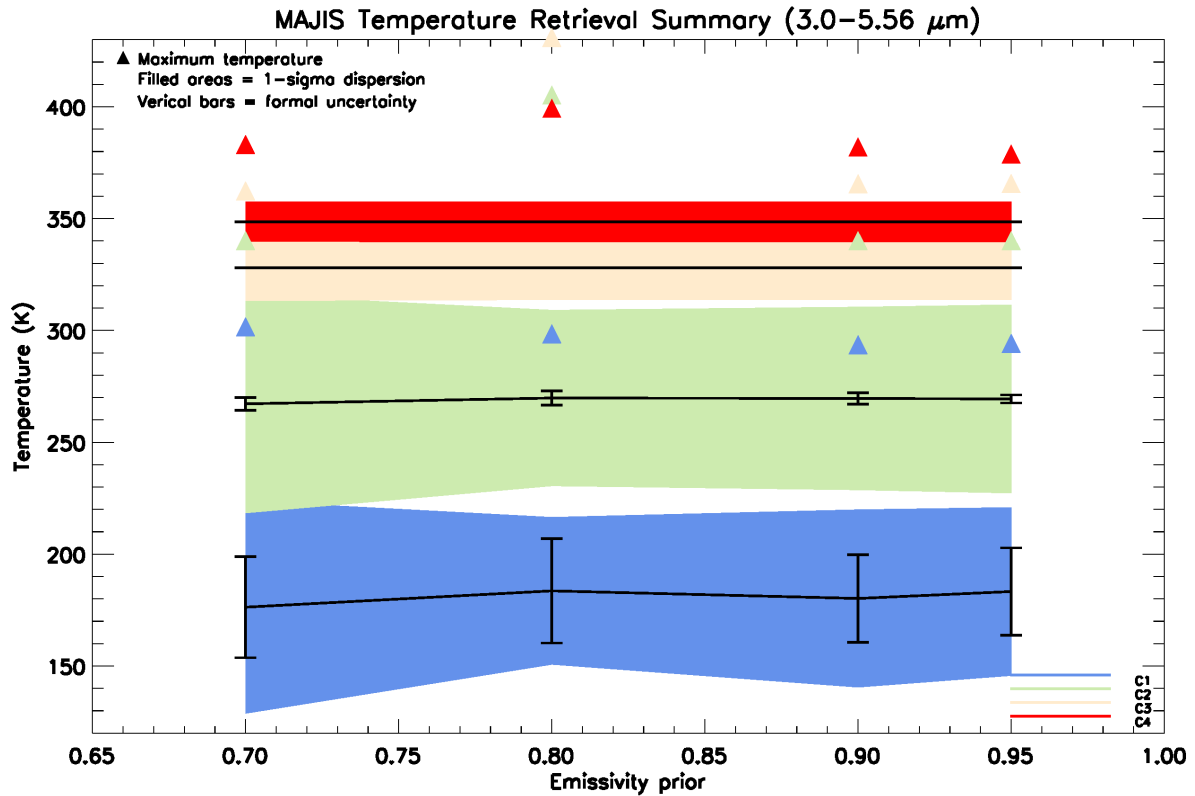


Figure 4. Summary of MAJIS temperature retrievals as a function of emissivity prior (3.0–5.56 μm spectral range). The coloured bands show the mean surface temperatures (solid lines) and corresponding $\pm 1\sigma$ dispersion for the four MAJIS observations (C1–C4), obtained from Bayesian inversion without photometric correction. Vertical black bars represent the mean formal uncertainties, and triangles indicate the maximum retrieved temperature values. Compared with the 4.5–5.56 μm case, the wider spectral interval yields similar temperature trends but generally lower formal uncertainties, especially under well illuminated conditions.

Results show that extending the lower bound of the spectral window from 4.5 to 3.0 μm produces a significant change in the character of the inversion (Figure 4 and Table A2). When using the full 3.0–5.56 μm range, the retrieval yields temperature values that are nearly invariant with respect to the emissivity prior, especially in the well illuminated datasets C3 and C4. In these cases, the mean surface temperatures converge to a fixed value regardless of the prior, and, while the associated 1– σ dispersion is substantially similar to the 4.5–5.56 μm case, the formal uncertainties collapse to zero, indicating that the inversion algorithm has converged to a narrow solution space (Figure 5). Although such tight convergence might suggest improved precision, it more likely reflects numerical over-constraint. This behaviour is consistent with an over-dominant contribution from shorter wavelengths—between 3.0 and 4.2 μm —where thermal emission is still weak and the radiance spectrum is more sensitive to the shape of the assumed reflectance curve and potential calibration uncertainties.

340

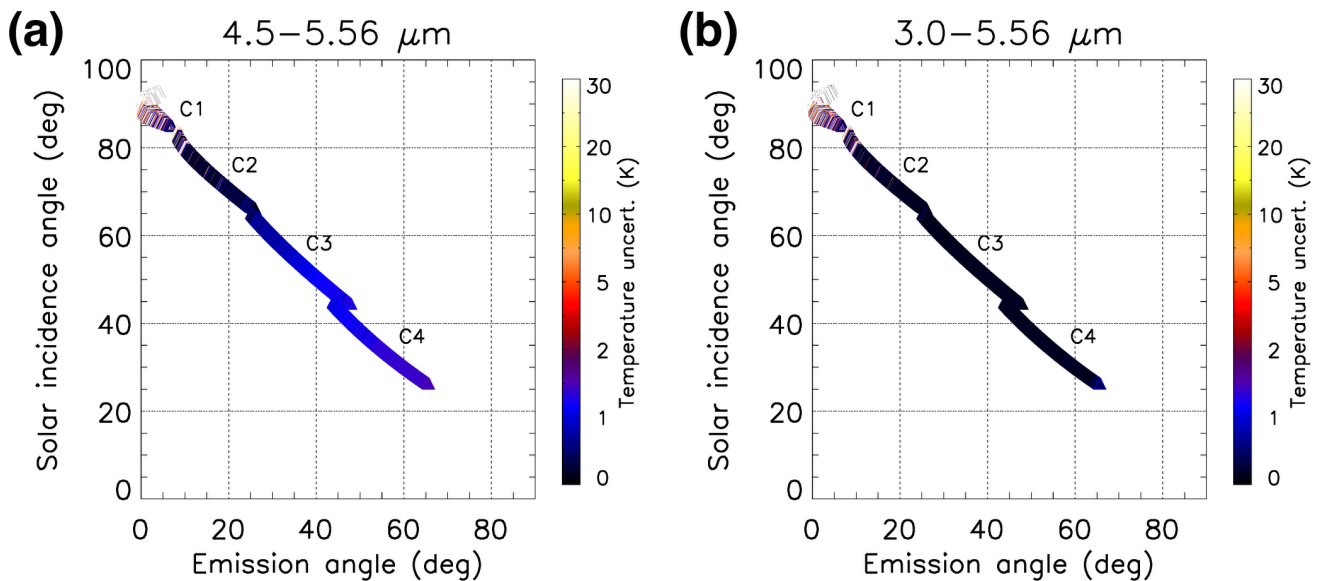


Figure 5. Formal uncertainties vs geometry. Formal uncertainties associated with the temperature values calculated in the four MAJIS acquisitions, as a function of the solar incidence angle (y -axis) and the emission angle (x -axis). Panels (a) and (b) refer to the retrieval cases in the range 4.5–5.56 μm and 3.0–5.56 μm , respectively. It can be noted that the wider spectral range results in a lower formal uncertainty under the same illumination and observation conditions for those data that benefit from full solar illumination.

Comparing corresponding rows across Tables A1 and A2 shows systematic differences in mean temperatures. For example, in C4 under $\epsilon_0 = 0.90 \pm 0.10$, the mean temperature increases from 345.2 K (4.5–5.56 μm) to 348.6 K (3.0–5.56 μm), while in C1 it decreases from 184.3 K (4.5–5.56 μm) to 180.2 K (3.0–5.56 μm). These small shifts reflect the different spectral leverage of the two wavelength ranges, as shorter wavelengths provide enhanced sensitivity to the thermal continuum at higher temperatures. In warm, well illuminated conditions, the additional thermal signal from the 3.0–4.5 μm interval strengthens the

350

fit to the observed radiance, improving the stability of the retrieval where the signal in the 4.5–5.56 μm range alone would begin to saturate.

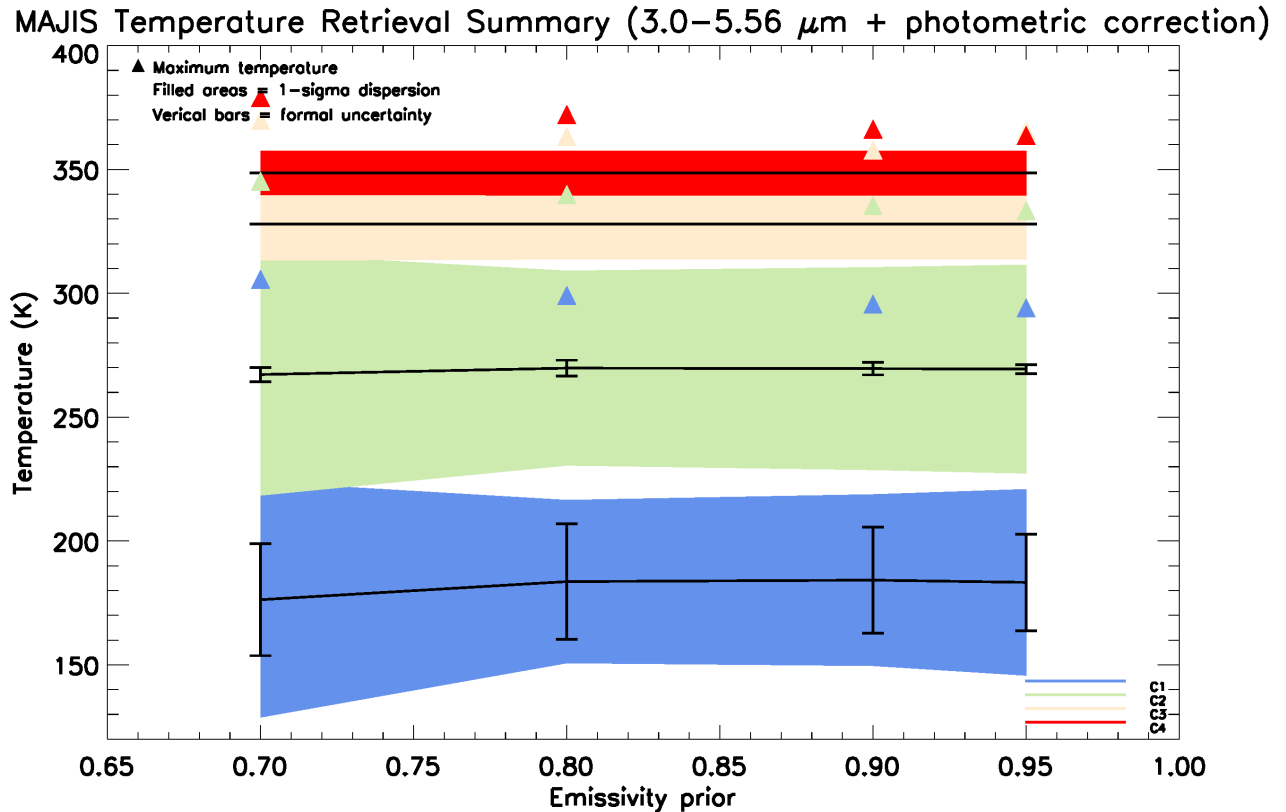
355 Despite these potential advantages, the retrieval from the broader 3.0–5.56 μm range may occasionally yield physically implausible outliers. For instance, in C3, a peak temperature of 430.9 K is reported under $\epsilon_0 = 0.80$ —a value well above what is expected for lunar surface conditions at that incidence angle. This suggests that residual artifacts or noise in the shortwave portion of the spectrum may corrupt the inversion under some conditions. These effects are not observed in the results from the 4.5–5.56 μm range, where temperature statistics behave smoothly and remain consistent with physical expectations.

360 Overall, these findings indicate that while the inclusion of wavelengths between 3.0 and 4.5 μm can, in principle, enhance retrievals in low-radiance scenes by increasing the spectral baseline, this benefit is offset by increased sensitivity to calibration uncertainties and reflectance modelling. In high-SNR, thermally bright observations such as C3 and C4, the narrower 4.5–5.56 μm range appears to offer more stable and physically reliable results. It minimizes sensitivity to the crossover region and avoids the numerical dominance of channels with mixed solar and thermal contributions.

365 These considerations support a context-dependent approach to spectral selection: the full 3.0–5.56 μm range may prove useful in cold or poorly illuminated scenes, whereas the more conservative 4.5–5.56 μm window is preferable when strong thermal emission is present. Future improvements in the treatment of solar reflectance and absolute calibration in the shortwave infrared may enable more confident use of the full range, but under current processing conditions, restricting the inversion to wavelengths dominated by thermal emission yields more robust and interpretable results.

370 A final test was performed by applying a Lommel–Seeliger photometric correction to the MAJIS spectra in the range 3.0–5.56 μm before retrieval, with the aim of reducing possible biases linked to viewing and illumination geometry. The Lommel–Seeliger law, originally formulated in the late 19th century to describe single scattering from dark planetary surfaces (Lommel, 1887; Seeliger, 1888), has long been applied to lunar observations as a simple and effective photometric correction. Its role was later formalized within the more general radiative transfer framework of Hapke (1981), where it is recognized as a limiting case particularly suited to the Moon’s porous regolith under moderate illumination conditions. The Lommel–Seeliger correction was implemented pixel-by-pixel through the factor $\mu/(\mu+\mu_0)$, where $\mu = \cos(i)$ and $\mu_0 = \cos(e)$ being i and e the solar incidence and emission angle, respectively, and normalizing the observed radiance to a canonical geometry ($i = 60^\circ$, $e = 30^\circ$) reproducing the high phase angle ($\sim 90^\circ$) of the JUICE lunar flyby. However, it is precisely this extreme phase angle that makes the correction sub-optimal, which explains why the retrieved temperatures (Figure 6 and Table A3) are virtually indistinguishable from those obtained without photometric adjustment. This outcome indicates that, within the spectral interval used for retrieval and at the spatial resolution of MAJIS, photometric effects have little influence on the thermal inversion. The Moon’s global shape can be approximated by a smooth ellipsoid at the few-hundred-meter pixel scale of MAJIS, so the primary driver of variability in the thermal signal is the distribution of insolation rather than geometric scattering. The Lommel–Seeliger law, while traditionally adopted for the diffuse scattering properties of the lunar regolith and effective at moderate phase angles where single scattering dominates, becomes less appropriate at the extreme phase angles encountered during the JUICE flyby. 385 In this geometry, multiple scattering, surface roughness, and shadowing effects grow increasingly important, and a single-

parameter correction cannot capture such complexity. The absence of significant differences between corrected and uncorrected retrievals is therefore unsurprising and further supports the robustness of the Bayesian thermal inversion under the observing conditions of the JUICE flyby.



390

Figure 6. Summary of MAJIS temperature retrievals as a function of emissivity prior (3.0–5.56 μm range, Lommel–Seeliger correction applied). The coloured bands indicate the mean surface temperatures (solid lines) and associated $\pm 1\sigma$ dispersion for the four MAJIS observations (C1–C4), derived from Bayesian inversion including the Lommel–Seeliger photometric correction. Vertical black bars show the mean formal uncertainties, and triangles mark the maximum retrieved temperature values. Compared to the uncorrected case, the photometric correction yields slightly smoother temperature trends and marginally reduced variability, especially across high incidence geometries.

395

For the subsequent intercomparison with the other methods (Section 2.5), we adopt the Bayesian retrieval parameters that provide the most physically plausible and stable results: the 4.5–5.56 μm spectral range, an emissivity prior of $\epsilon_0 = 0.70 \pm 0.15$, and no photometric correction.

400

2.2 Empirical thermal correction

Li and Milliken (2016) developed an empirical thermal correction model tailored for spectra acquired by the Moon Mineralogy
405 Mapper (M^3), which operated over the spectral range 0.43–3.0 μm (Pieters et al., 2009). They identified that at wavelengths
beyond $\sim 2 \mu\text{m}$, thermal emission from the lunar surface contributes significantly to the measured radiance, particularly on the
dayside. This thermal component can obscure or distort diagnostic absorption features associated with minerals and hydration,
rendering accurate compositional analysis challenging.

To address this, they constructed a model grounded in laboratory measurements of lunar soils and glasses, leveraging the
410 strong empirical correlation between reflectance at 1.55 μm (unaffected by thermal emission) and at 2.54 μm (where thermal
emission may be substantial, depending on the surface temperature). This relationship follows a power law, enabling the
prediction of the “true” reflectance at 2.54 μm based on the value at 1.55 μm . Any excess radiance at 2.54 μm is attributed to
thermal emission, which can then be quantified and removed. Crucially, this approach allows for simultaneous estimation of
the surface temperature, without requiring independent thermal measurements from instruments like Diviner, provided the
415 observed materials match common lunar regolith compositions.

This method is particularly useful when applied to MAJIS data acquired in its visible and near-infrared (VISNIR) channel
covering the spectral range 0.49–2.36 μm . While this does not extend as far into the thermal regime as M^3 (and the MAJIS-IR
channel itself), thermal contributions can still become non-negligible near the upper end of this spectral window—especially
for observations near local noon or in equatorial regions. Applying the Li and Milliken (2016) model to MAJIS data enables
420 the detection and removal of this thermal component, improving the fidelity of the retrieved reflectance spectra. In doing so,
it not only enhances mineralogical interpretations in the near-IR but also yields estimates of surface temperature derived
directly from the observed radiance, assuming that a portion of the MAJIS spectrum captures the onset of thermal emission.
This makes the approach particularly attractive for MAJIS lunar observations where Diviner-like thermal constraints may be
unavailable or spatially mismatched, while allowing a direct comparison with the Bayesian method.

425 By grounding the correction in the inherent spectral behaviour of lunar soils and leveraging the statistical predictability of
thermally unaffected wavelengths, this model provides a robust and computationally efficient tool for disentangling thermal
and reflective components in hyperspectral datasets such as those from MAJIS.

Formally, the method proposed by Li and Milliken (2016) relies on two main equations. The first is Kirchhoff’s law of radiative
equilibrium:

430

$$I = 1/\pi F_{\text{Sun}} R + I_{\text{BB}}(T)(1-R) \quad (2)$$

where I is the total radiance emitted by the surface, F_{Sun} the solar irradiance received by the surface, I_{BB} the blackbody radiance at temperature T associated with the surface thermal emission, and $R = 1 - \varepsilon$ the surface reflectance, which is related to the emissivity ε under radiative equilibrium. The second equation is an empirical power-law relationship between the reflectances at 1.55 μm and 2.54 μm , measured in the laboratory on lunar soil and glass samples under the geometry $i = 30^\circ$, $e = 0^\circ$:

$$R_{2.54} = 1.124 \times R_{1.55}^{0.8793} \quad (3)$$

Assuming that thermal emission is negligible at 1.55 μm , i.e., $I_{1.55} \approx 1/\pi F_{\text{Sun}} R_{1.55}$, the thermal emission of the surface—and therefore its temperature—can be directly derived from the radiances measured by MAJIS at 1.55 and 2.54 μm , together with the incoming solar flux, without requiring additional assumptions about the surface emissivity. This makes the method computationally very efficient.

Nevertheless, over the range of lunar surface temperatures, the radiance excess at 2.54 μm can be small or even undetectable due to the radiometric uncertainty of MAJIS (see Langevin et al., this issue), which tends to scatter data points around the power-law curve (Figure 7). Consequently, all data points lying below the power-law relation correspond to surface temperatures that cannot be reliably estimated—or are highly uncertain—using this empirical approach. This limitation is most pronounced near the terminator (e.g., in C2), where thermal emission is weak and radiometric uncertainties dominate.

To assess the accuracy of the surface temperature estimates, in Figure 7 we compare our results with those predicted by the two-layer thermal equilibrium model proposed by Vasavada et al. (1999), with updated parameters based on LRO/Diviner observations (Vasavada et al., 2012). Our surface temperature estimates show good agreement with the model for solar incidence angles below 55° but diverge significantly at higher incidence angles. ~~This discrepancy likely arises from unresolved topographic effects, which are not accounted for when data are georeferenced to a smooth ellipsoid.~~ This discrepancy likely arises from unresolved sub-pixel topographic effects (e.g. mixed slopes and shadowing) that are not represented in the ellipsoid-based geometry and can locally bias the measured radiance. Sub-pixel slopes and shadowing can dominate the measured radiance and produce local deviations from the expected thermal behavior. In the MAJIS observations, this incidence range corresponds to the highlands observed at the end of C3 and the beginning of C4. ~~Part of the observed differences may also reflect the intrinsic mismatch between the MAJIS physical-temperature retrieval and the Diviner brightness-temperature products used for comparison.~~ In terms of accuracy, assuming a 10% uncertainty in the radiometric flux measured by MAJIS, the corresponding uncertainties in surface temperature are estimated at ± 15 K for C2, ± 7 K for C3, and ± 5 K for C4.

The Li and Milliken (2016) method also allows for an a posteriori determination of emissivity at 5.5 μm by inverting Kirchhoff's law, under the assumption that reflected sunlight at this wavelength is negligible, i.e., $I_{5.5} \approx \varepsilon_{5.5} I_{\text{BB}}(T)$. This capability will be further exploited in subsection 2.5.2, where emissivity retrievals obtained with different approaches are compared in detail.

465

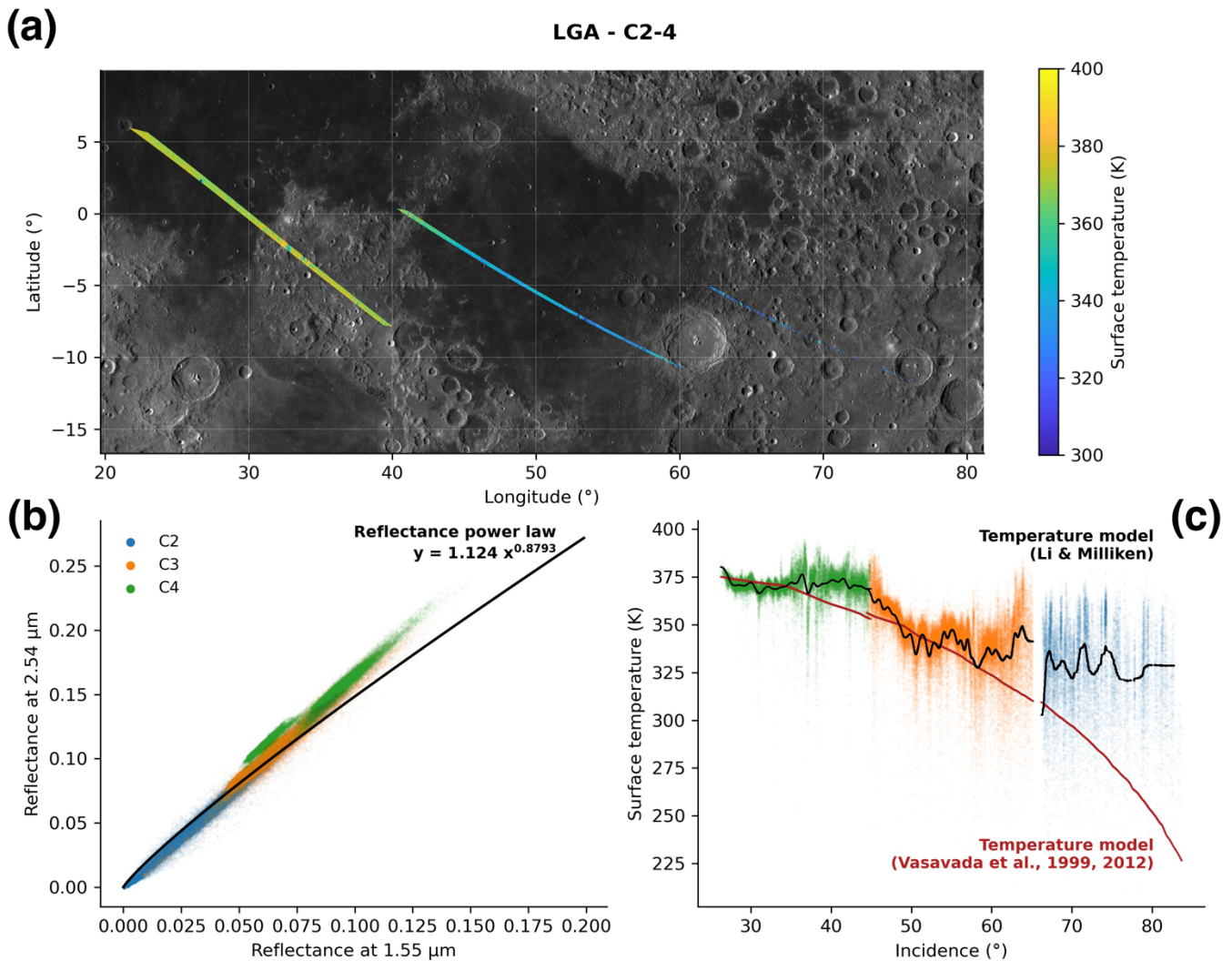


Figure 7. Empirical thermal correction results. Lunar surface temperature estimates on the MAJIS' C2–4 observations. **(a)**: map of the temperature along MAJIS' tracks. Background image: Moon LRO LROC WAC Global Morphology Mosaic 100m, June 2013 (Speyerer et al., 2011; Wagner et al., 2015). **(b)**: reflectance at 2.54 μm as a function of the reflectance at 1.55 μm illustrating the power law relation established by Li and Milliken (2016). Points above the black curve correspond to a “reflectance excess” due to thermal emission. **(c)**: derived surface temperature and its median (black line) as a function of solar incidence. The red curve is the Vasavada et al. (1999, 2012) temperature model during the lunar day.

2.3 Roughness-informed thermal model

475 An additional approach builds upon the roughness-informed model introduced by Wohlfarth et al. (2023), originally developed to improve our understanding of the lunar diurnal water cycle based on M³ observations. ~~In this work, the framework is~~

specifically adapted to MAJIS data with the goal of retrieving surface temperature and emissivity, rather than performing a full thermophysical inversion. We adopt the treatment of both the reflectance and thermal-emission components as described by Wohlfarth et al. (2023). In this framework, the reflectance contribution is modelled according to the Hapke formalism (Hapke, 2005), adopting the set of Hapke parameters reported by Li and Li (2011), whereas the thermal-emission component is implemented following the approach detailed in Wohlfarth et al. (2023). We note, however, that under the high phase-angle conditions of the JUICE lunar flyby ($\sim 90^\circ$), no photometric formulation can be regarded as strictly optimal, including Hapke-based corrections; in the present implementation, the Hapke term should therefore be viewed as a physically motivated approximation of the reflectance contribution rather than as a unique or fully constrained solution.

480

Unlike purely empirical approaches, the model represents sub-pixel roughness in terms of RMS slope using synthetic fractal surfaces (Rozitis et al., 2020). These surfaces statistically reproduce unresolved topographic variability at the cm–mm scale and allow the simulation of associated effects such as self-heating, sub-pixel shadowing, and multiple scattering.

485

~~Unlike empirical approaches, this model explicitly accounts for local topography through a fractal surface formulation that includes self-heating, self-scattering, sub-pixel shadowing, and bolometric albedo.~~ In this fractal representation, the surface is

490

depicted as a series of discrete square plates, called “*facets*.” The model solves the energy balance for each facet m , where the total flux F_m is the sum of three components: direct solar irradiation, scattered sunlight, and thermal self-heating from other facets. In our case, we divide each MAJIS pixel into a 65×65 sub-pixel grid, where the thermal balance is computed individually. The resolution of the sub-pixel facets provides a good compromise between capturing sub-pixel temperatures and computational tractability.

495

Once a sub-pixel synthetic fractal roughness surface is generated ~~for each pixel and the DEM derived and the effective solar incidence and emission angles are defined~~, the thermal contribution of the m -th sub-pixel facet is given by the energy balance equation:

$$F_m = F_m^{sun} + F_m^{sca} + F_m^{rad} \quad (4)$$

500

where F_m^{sun} is the flux of directly absorbed solar radiation, F_m^{sca} is the contribution of scattered sunlight from neighbouring sub-pixel facets and F_m^{rad} is the additional flux due to thermal self-heating. The thermal emission related to direct solar irradiation of the m -th sub-pixel facet is modelled as:

505

$$F_m^{sun} = (1 - A_{dh})J_m \quad (5)$$

where A_{dh} is the directional–hemispherical albedo ~~for the reflected sunlight (Shkuratov et al., 2011), here computed for each pixel following the workflow of Wöhler et al. (2017) and intrinsically connected to the single-scattering albedo, which is a free parameter of the model, while~~ J_m is the incident solar irradiance on the m -th sub-pixel facet. The terms for scattering

510 from neighbouring sub-pixel facets (F_m^{sca}) and thermal self-heating (F_m^{rad}) are respectively:

$$F_m^{sca} = (1 - A_{dh})A_{dh} \sum_{j \neq m}^{65 \times 65} f_{m,j} J_j + (1 - A_{dh})A_{dh}^2 \sum_{j \neq m}^{65 \times 65} f_{m,j} \sum_{k \neq j}^{65 \times 65} f_{j,k} J_k + \dots \quad (6)$$

$$F_m^{rad} = (1 - A_{dh,th}) \sum_{j \neq m}^{65 \times 65} f_{m,j} F_j + (1 - A_{dh,th})A_{dh,th} \sum_{j \neq m}^{65 \times 65} f_{m,j} \sum_{k \neq j}^{65 \times 65} f_{j,k} F_k + \dots \quad (7)$$

515

where $f_{i,j}$ are the geometric view factors (Wohlfarth et al., 2023) and $A_{dh,th}$ is the **directional hemispherical albedo for self-heating** (Wohlfarth et al., 2023), which is linked to the effective emissivity ε by Kirchhoff's law (Spencer, 1990). The reported equations are resolved in a matrix-vector notation to account for higher order terms for F_m^{sca} and F_m^{rad} , following the pipeline described by Wohlfarth et al. (2023). Subsequently, the Stefan–Boltzmann law relates the radiant flux of the m -
520 th sub-pixel facet F_m to its equilibrium temperature, which can be retrieved jointly with the effective emissivity ε :

$$T_m = \left(\frac{F_m}{\varepsilon \sigma} \right)^{\frac{1}{4}} \quad (8)$$

525 Once the temperatures of the sub-pixel facets are estimated, the thermal emission component linked to the n -th pixel is defined as:

$$X_n(\lambda) = \frac{\sum_m^{65 \times 65} P_m(\lambda) v_m \cos e_m}{\sum_m^{65 \times 65} v_m \cos e_m} \quad (9)$$

530 where $P_m(\lambda)$ denotes the Planckian thermal emission of the m -th sub-pixel facet, computed from its estimated equilibrium temperature; v_m is a line-of-sight visibility factor to the sensor and e_m is the emission angle of the m -th sub-pixel facet. The retrieval is performed in the **5.0–5.5 μm** spectral range, which is dominated by thermal emission and largely unaffected by detector saturation. ~~Within this range, the emissivity is assumed to be spectrally constant. An initial value of $\varepsilon=0.95$ is adopted, consistent with previous studies on lunar regolith (Bandfield et al., 2015; Bandfield et al., 2018) and subsequently allowed to vary together with surface temperature.~~ At this stage, single scattering albedo is optimized by minimizing the root mean square
535 error (RMSE) between the modelled **reflected radiance plus** thermal emission $X_n(\lambda)$ and the observed MAJIS spectra. ~~The simulations are not performed on a pixel-by-pixel basis because the computational cost would be prohibitive, even under aggressive parallelization. Instead, we construct a three-dimensional grid whose axes correspond to the effective incidence angle i , the emission angle e , and the macroscopic roughness ρ_{rough} . The internal spacing of the grid is set to steps of ($\Delta i=0.5^\circ$; $\Delta e=0.5^\circ$; $\Delta \rho_{\text{rough}}=0.02$). This discretized grid allows temperatures to be evaluated only for the ($i, e, \rho_{\text{rough}}$)~~
540 ~~combinations that occur within the hyperspectral cube. This approach avoids repeated computations for near duplicate configurations that would yield comparable results and substantially reduces the overall computational cost. Because the phase~~

angle for all four hyperspectral cubes is $\sim 90^\circ$ with minimal variability (on the maximum order of $\pm 2^\circ$ with respect to its average value), it is not included as a fourth grid dimension. Instead, the mean phase angle for each $(i, e, \rho_{\text{rough}})$ combination is adopted as a fixed value in the simulations.

545 The synthetic fractal surfaces are generated by using as free parameter the sub-pixel cm–mm scale roughness. However, applying a full coupled reflectance–thermal inversion based on synthetic fractal surfaces on a pixel-by-pixel basis over the entire hyperspectral cubes would be computationally demanding and, more importantly, not warranted by the information content of all datasets. We therefore retrieve representative average sub-pixel roughness values only for selected regions of interest (ROIs), chosen to sample the main terrain units.

550 In particular, we use the C4 radiance dataset for the roughness retrieval because this hyperspectral cube provides the most favorable illumination geometry and the strongest thermal contribution. As a result, the modeled radiance exhibits the highest sensitivity to sub-pixel roughness. In contrast, for cubes C1 and C2 the thermal signal is comparatively weak and the measured radiance is largely dominated by noise. This prevents a robust constraint on surface roughness and introduces a strong degeneracy with the single-scattering albedo. For this reason, retrieving roughness independently for C1 and C2 would lead to
 555 poorly constrained solutions with limited physical interpretability. Instead, we adopt the terrain-representative roughness values derived from the C4 cube for the analysis of the other datasets.

Nevertheless, degeneracies intrinsic to thermophysical models may still affect the retrieval even for C4. To assess and mitigate this effect, we performed 20 independent simulations for each ROI, varying the initial guesses for both roughness and single-scattering albedo. These simulations generally converge to slightly different solutions without any evident outlier, which can
 560 be used to estimate the uncertainties of the retrieved parameters and to evaluate the impact of model degeneracy. Within this framework, the sub-pixel roughness is found to be well constrained, whereas the single-scattering albedo shows a maximum variability of about 20% within both ROIs.

The ROIs used to constrain the sub-pixel roughness, cm-mm scale roughness, and single-scattering albedo at $5.5 \mu\text{m}$ for the C4 hyperspectral cube are listed in Table 2. The retrieved sub-pixel roughness values are subsequently compared with
 565 macroscopic roughness estimates derived from the LOLA Digital Roughness Map (LRO/LOLA LDRM_32 data) (Smith et al., 2010, 2017). These values are expressed as terrain RMS slope and are shown in Figure 8, while the average values for the corresponding ROIs are reported in Table 2.

Table 2. Terrain type, geographic coordinates, retrieved sub-pixel roughness, and single-scattering albedo for the specific ROIs defined to
 570 derive average values of sub-pixel-scale roughness.

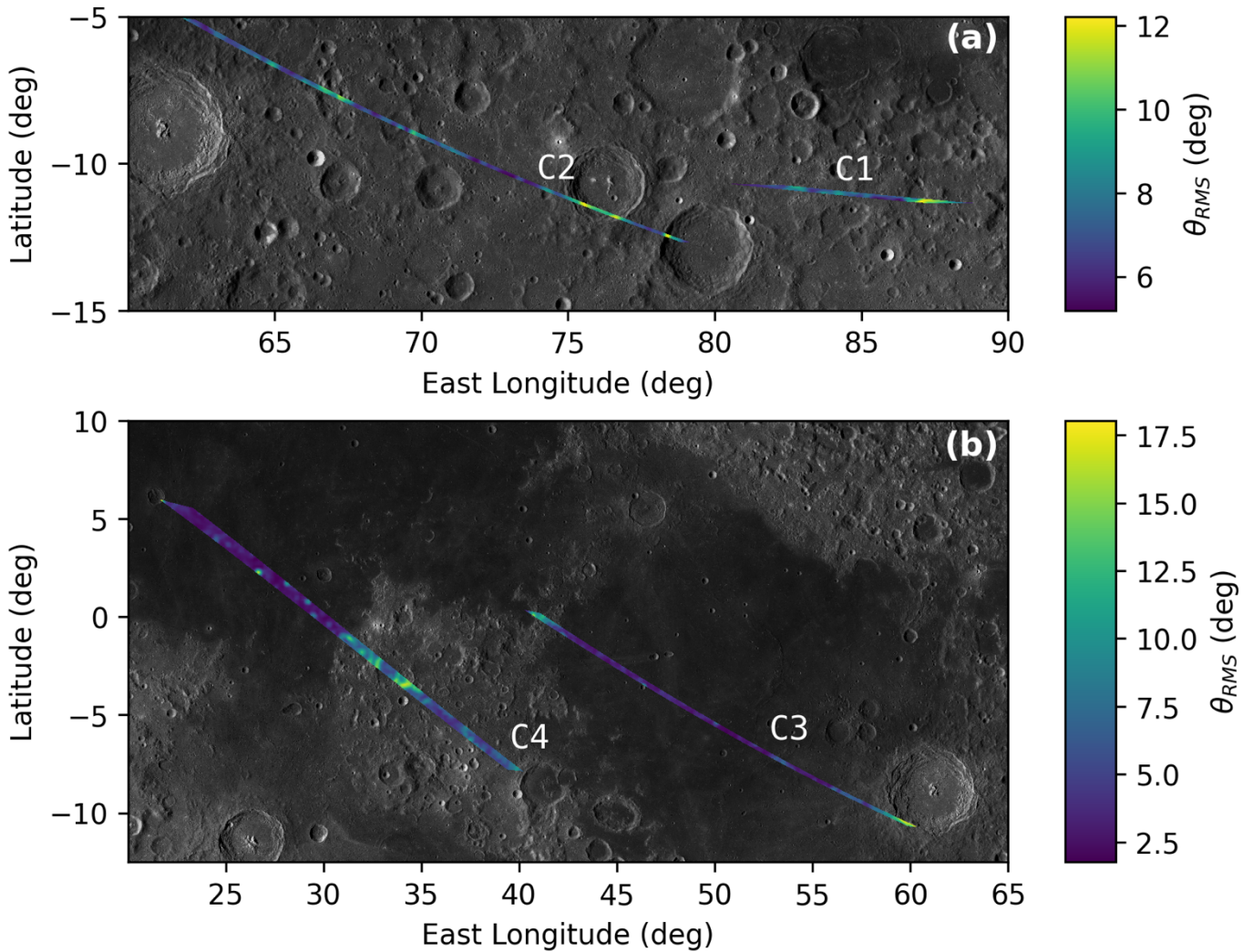
Terrain type / hyperspectral cube	Geographical context of the ROI	Average sub-pixel roughness (θ_{RMS})	Average roughness LRO/LOLA (θ_{RMS})	Single-scattering albedo ($\omega_{5.5\mu\text{m}}$)
Mare-like / C4	3.5°—5.0°N 23.7—25.1°E	$(20.64^\circ \pm 0.91^\circ)$	$(3.31^\circ \pm 0.88^\circ)$	(0.55 ± 0.10)

Highland-like / C4	3.0—4.3°S 32.5—35.5°E	$(26.97^\circ \pm 2.66^\circ)$	$(9.88^\circ \pm 3.40^\circ)$	(0.59 ± 0.10)
--------------------	--------------------------	--------------------------------	-------------------------------	-------------------

575 We assume that the average sub-pixel roughness retrieved and reported in Table 2 are representative for the corresponding terrain units (maria-like and highlands-like) for the C1–C4 hyperspectral cubes. The sub-pixel roughness values are expected to be comparable within the JUICE/MAJIS footprints, consistent with the behaviour observed across the lunar surface, as indicated by previous studies (e.g., Wohlfarth et al., 2023). With this approach, we account for realistic average sub-pixel roughness values across different terrain types while avoiding a full pixel-by-pixel retrieval, which would be computationally expensive and strongly affected by parameter degeneracy in low-SNR hyperspectral cubes, as for C1 and C2. ~~To match the spatial resolution of MAJIS cubes, they have been interpolated using a Gaussian filter (Figure 8). This procedure yields slope distributions that are statistically consistent with pixel scale roughness, avoiding implementations based on arbitrary assumptions or retrieved values of roughness. This approach reduces the risk of degeneracies among free parameters, which in this case are limited to pixel emissivity and temperature.~~ Results indicate that the average sub-pixel roughness values are overall higher in terms of RMS slope than those inferred at the meter scale. This outcome is consistent with expectations from previous studies (e.g., Rubanenko et al., 2020) and falls within the 20°–35° range reported in earlier analyses based on near-nadir Diviner observations (Bandfield et al., 2015) and TIR spectral data (Rubanenko et al., 2020; Müller et al., 2021;

 580 ~~Wohlfarth et al., 2023).~~ In addition, effective incidence angles are computed by combining the observing geometry with local terrain slopes from LOLA Digital Slope Map (LRO/LDSM_16 data) (Smith et al., 2010, 2017), thereby better reproducing the actual physical illumination conditions (Figure 9).

 585



590 **Figure 8. LOLA-derived roughness maps.** Estimated large-scale roughness (**RMS slope**) derived from LDRM_32 LRO/LOLA data, interpolated with a Gaussian filter to match the spatial resolution of the four MAJIS observations: (a) C1 and C2; (b) C3 and C4. **The estimated pixel-scale roughness values have been employed as a priori surface parameters to constrain the temperature estimation within the roughness-informed model approach.** Background image: Moon LRO LROC WAC Global Morphology Mosaic 100m, June 2013 (Speyerer et al., 2011; Wagner et al., 2015).

595

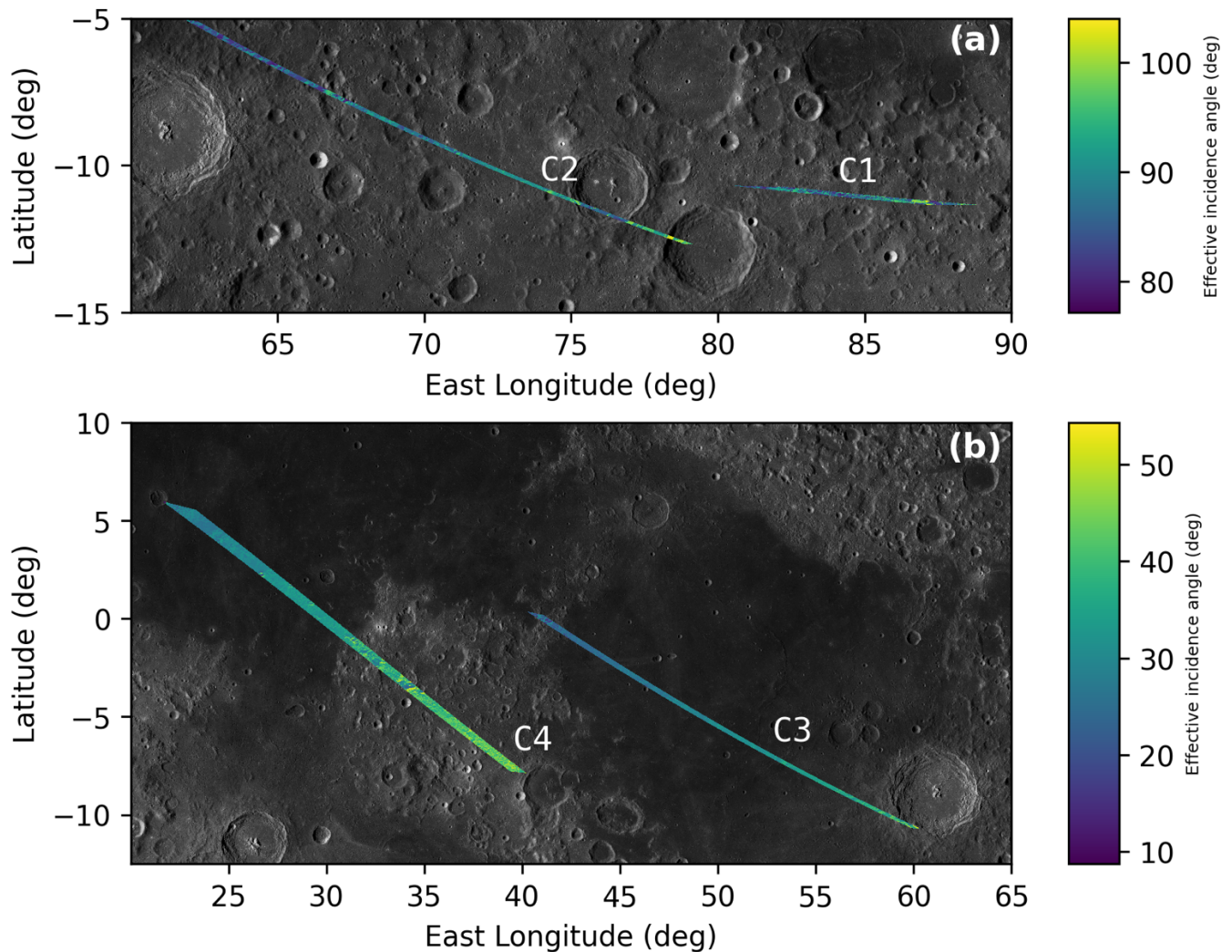
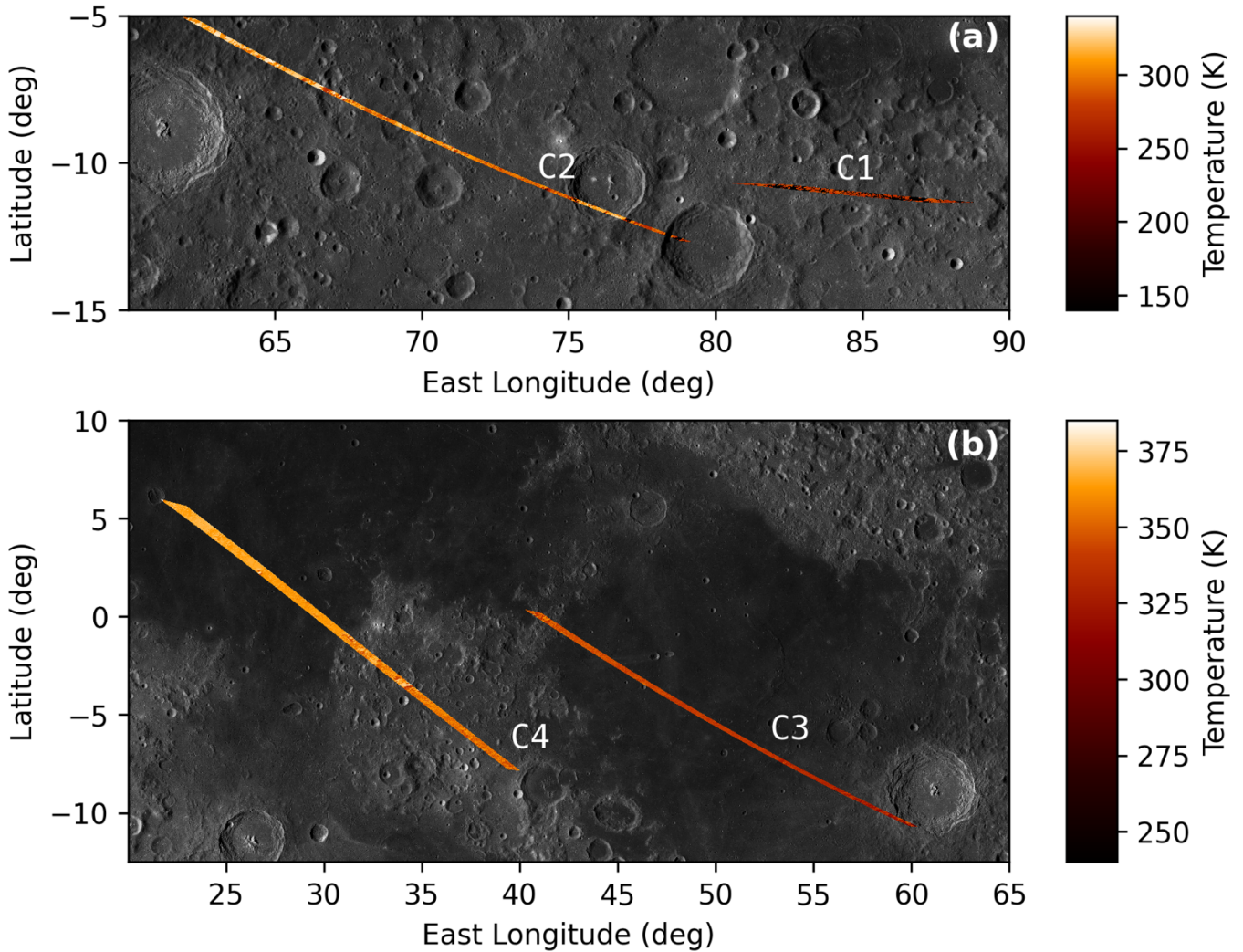


Figure 9. Effective solar incidence angles. Effective incidence angles derived combining the observational geometries with the local terrain slopes from LDSM_16 LRO/LOLA data, convolved to match the spatial resolution of the MAJIS observations: (a) C1 and C2; (b) C3 and C4. The variability associated with local topography is most evident in C1 and C2, where the altimetric variations measured by LRO/LOLA significantly alter solar incidence across rugged terrains. Background image: Moon LRO LROC WAC Global Morphology Mosaic 100m, June 2013 (Speyerer et al., 2011; Wagner et al., 2015).

After constraining the sub-pixel cm–mm scale roughness in specific ROIs (Table 2), temperatures retrieved from each MAJIS hyperspectral cube are reported in Figure 10. The retrieved temperatures exhibit a clear spatial correlation with both macroscopic surface roughness (Figure 8) the effective illumination conditions (Figure 9). The highest temperature value (385 383 K) is observed in the northwestern sector of C4, consistent with the local incidence angles and in agreement with the location of maximum temperature identified by the other two methods. Furthermore, low-albedo terrains exhibit higher

610 surface temperatures than brighter terrains at the same local solar time. This behavior is evident in the transition region between Mare Tranquillitatis and the adjacent highland-like terrain in C4 (Figure 10). Conversely, the lowest temperature values (<150 K) occur in shadowed regions of C1 and C2, corresponding to pixels characterized by effective incidence angles exceeding 90° (Figure 10).

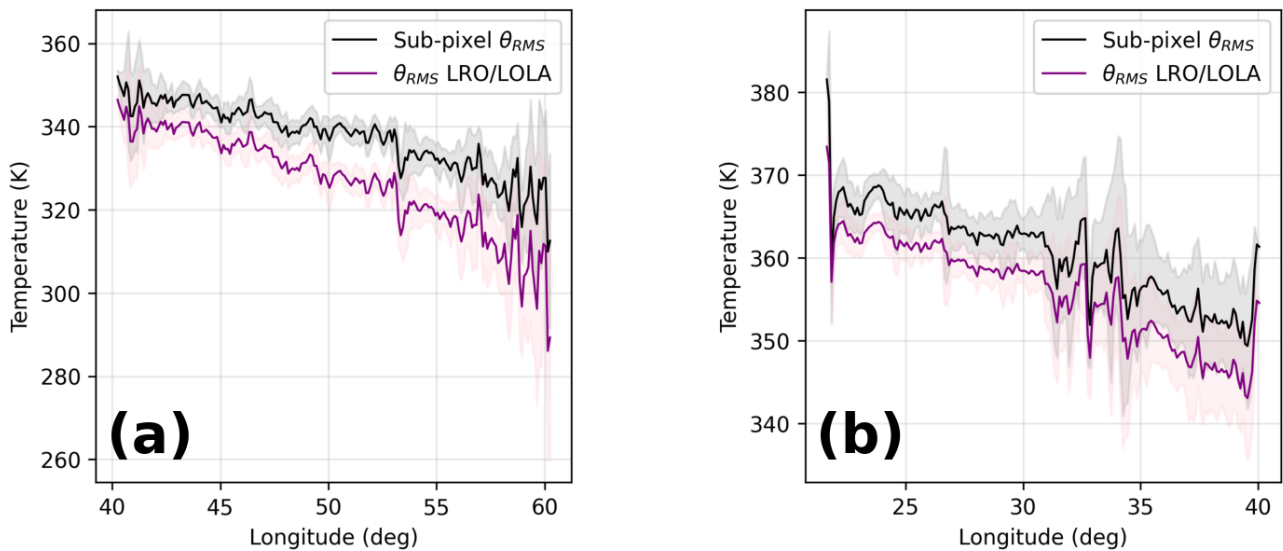


615 **Figure 10. Temperatures from roughness-informed model.** Temperatures retrieved using the roughness-informed thermal model: (a) C1 and C2; (b) C3 and C4. Spatial variations in the temperatures are primarily controlled by both surface roughness (Figure 8) and the effective illumination conditions (Figure 9) and sub-pixel cm-mm scale roughness (Table 2). The maximum temperature value (383 K) is observed in the northwestern portion of C4, whereas the lowest values (<150 K) occur in C1 and C2, within areas strongly affected by local topographic shading, corresponding to non-illuminated surfaces ($i > 90^\circ$), as highlighted in Figure 9. Background image: Moon LRO LROC WAC Global Morphology Mosaic 100m, June 2013 (Speyerer et al., 2011; Wagner et al., 2015).

Accounting for macroscopic sub-pixel roughness, as opposed to adopting the macroscopic roughness measured by LRO/LOLA, introduces only modest though measurable variations in the retrieved temperatures. For this reason, here we use the approach macroscopic roughness measured by LRO/LOLA even under identical illumination geometries. Here, the analysis focuses on C3 and C4, which provide the most favourable illumination conditions. For each observation, polynomial functions are fitted to the temperatures as a function of the effective incidence angle (Figure 11), and the resulting best fit curves are grouped into subcategories representative of distinct macroscopic roughness classes. In general, temperatures increase with roughness, with the largest variability occurring near an incidence angle of 55° . At higher incidence angles, the growing role of local topography (Figure 11a) is consistent with the deviations observed in the empirical approach relative to the Vasavada model (Figure 7), highlighting that neglecting topographic effects—and thus thermal beaming (Spencer, 1990; Rozitis and Green, 2011)—introduces systematic biases in temperature retrievals. This trend should, however, be interpreted with caution, as the roughness-temperature relationship is also likely modulated by factors not explicitly considered in this analysis, including true sub-pixel topography, surface composition, and wavelength-dependent emissivity.

To further assess the influence of roughness assumptions, we perform a similar analysis by assuming the sub-pixel roughness to be equal to the meter-scale roughness measured by LRO/LOLA (Figure 8). This test is intended to evaluate the similarities and differences in the resulting temperature estimates.

In our case, the sub-pixel roughness at the cm-mm scale is significantly higher than the macroscopic roughness (Table 2), which may lead to different contributions from self-heating, self-shadowing, and scattered sunlight. A direct comparison between the temperatures retrieved under the two assumptions for C3 and C4 is shown in Figure 11.



640 **Figure 11. Effect of macroscopic roughness on retrieved surface temperatures (C3–C4).** Surface temperature variations computed using the average sub-pixel roughness value (black line) and the macroscopic roughness values derived from LRO/LOLA data (purple line) for the sub-pixel fractal surface generation, shown for C3 (a) and C4 (b). The shaded areas correspond to the $1\text{-}\sigma$ dispersion after binning with a longitudinal step of 0.1° .

645 The results shown in Figure 11 highlight the differences between a full thermophysical inversion, in which the average sub-pixel roughness is retrieved, and the assumption that cm–mm scale roughness matches the macroscopic roughness derived from LRO/LOLA measurements (Figure 9). Within the longitude range between 22.5° and 46.0° , the retrieved temperatures are partially comparable within the associated uncertainties—defined as the $1\text{-}\sigma$ dispersion after binning the data with a longitudinal step of 0.1° —although temperatures derived using the cm–mm scale roughness are on average slightly higher.

650 This result suggests that self-heating, self-shadowing, and scattering effects are mitigated—and therefore less sensitive to surface roughness—at low incidence angles, as expected from previous studies (Spencer, 1990; Wohlfarth et al., 2023). For longitudes beyond 46.0° , the two approaches begin to diverge (Figure 11), with temperature differences exceeding the associated uncertainties and therefore no longer comparable within the $1\text{-}\sigma$ error bars. In particular, the skin temperature retrieved using the sub-pixel roughness values derived from the thermophysical modeling (Table 2) is systematically higher

655 than that obtained when assuming that the macroscopic roughness derived from LRO/LOLA matches the sub-pixel roughness at the cm–mm scale. This behavior indicates that the terms dominating Eq. 4 become increasingly sensitive to micro-scale slopes at higher incidence angles. Higher roughness values correspond to steeper slopes at the cm–mm scale, which enhance the radiative interaction between facets and increase the contribution of the self-heating term, as expected (Spencer, 1990). The largest variation is observed for C3 at longitude of 56.2° , corresponding to a temperature difference of $(15.3\text{ K} \pm 11.8\text{ K})$.

660 The spatial distribution of the temperature differences between the two assumptions is reported in Figure A2.

2.4 Cross-wavelength comparison with LRO/Diviner

To place the MAJIS thermal observations into a broader lunar context, we compared our results with co-located datasets from the Diviner Lunar Radiometer Experiment aboard LRO (Williams et al., 2017). Diviner provides radiance and brightness

665 temperature for channels 3–6 ($7.8\text{--}25\ \mu\text{m}$), along with derived emissivity maps and the Christiansen Feature (CF) wavelength. For this work, we gathered Diviner radiances for channels 3–6 acquired under sub-solar longitudes between -26° and $+18^\circ$. Following Williams et al. (2018), the field of view of each measurement was modelled using a Monte-Carlo distribution of 50 points to compute its effective footprint.

Radiances were then adjusted to the solar distance corresponding to the JUICE flyby (1.014 au) under the assumption of

670 radiative equilibrium, and subsequently gridded at 128 pixels per degree. Because Diviner does not provide full spatial coverage at the exact solar geometry of the MAJIS observations (sub-solar longitude -4.1° , sub-solar latitude 1.0°), we estimated gap-free radiances by linearly interpolating the observations bracketing each pixel in sub-solar longitude. This

procedure reproduces the large-scale thermal structure well, though orbit-to-orbit striping remains visible in places (Figure 12). CF position and peak brightness temperature were determined by parabolic fitting of channels 3, 4 and 5 (Greenhagen et al., 2010 ~~Williams et al., 2018~~), and channel emissivities were evaluated relative to the CF peak temperature. We note that Diviner products provide brightness-temperature quantities (including the peak brightness temperature around the CF) rather than a direct estimate of physical thermodynamic surface temperature. In this work, the Diviner peak brightness temperature is used as a practical proxy for the surface thermal state, since it is derived near the CF where the effective emissivity is expected to be close to unity and the dependence on emissivity is reduced compared to single-channel brightness temperatures.

675
680 This approach highlights compositional and textural contrasts between mare and highlands, although emissivity estimates at large incidence angles ($i > 60^\circ$) are strongly affected by photometric roughness effects, particularly in channel 6.

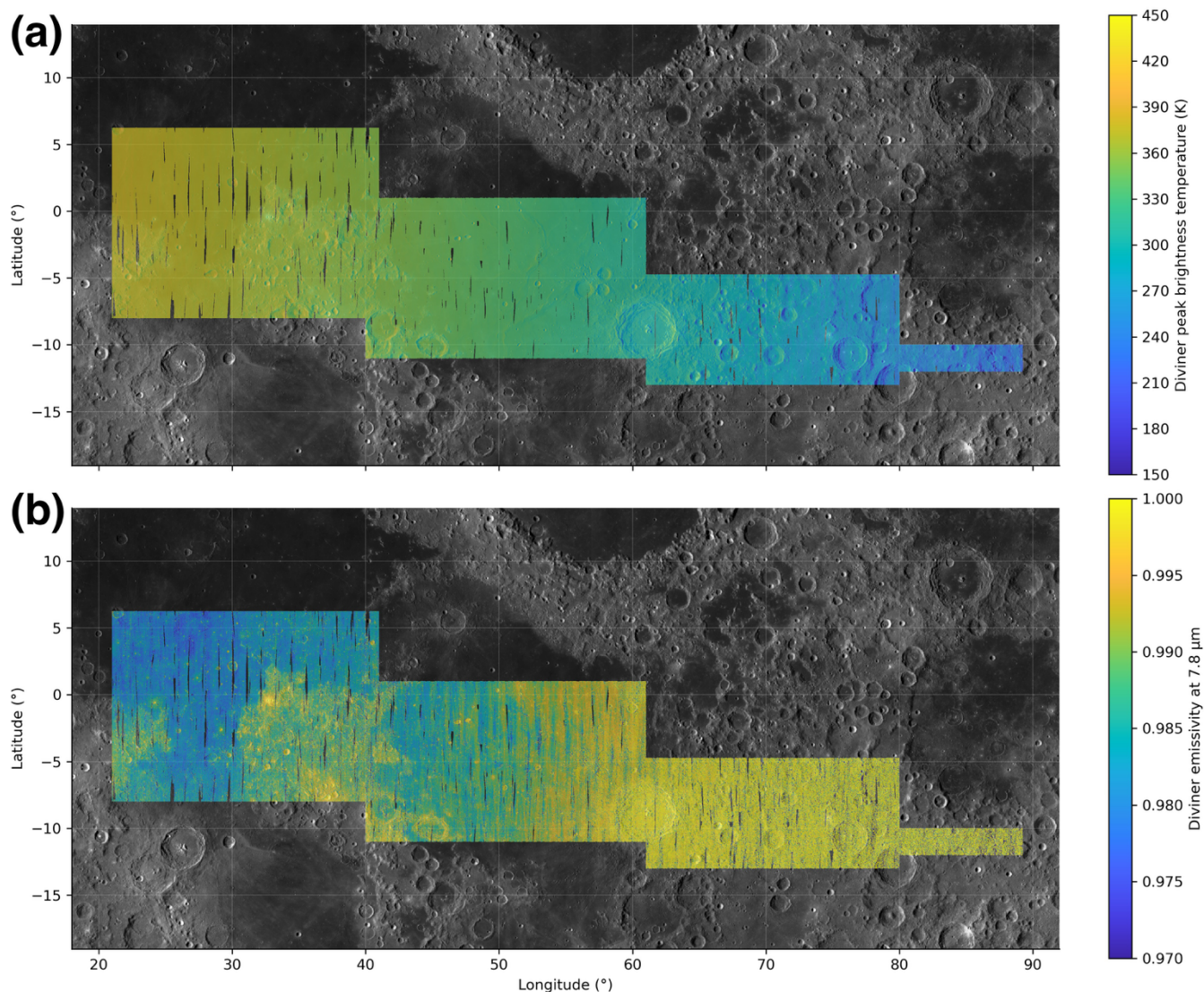


Figure 12. Diviner brightness temperature and emissivity. (a) Diviner peak brightness temperature (channels 3–6, 7.8–25 μm) over the MAJIS ground track, gridded at 128 px/degree (~240 m/px at the equator) and interpolated across adjacent sub-solar longitudes to match the illumination of the JUICE flyby. The map captures the large-scale thermal contrast between Mare Tranquillitatis and the surrounding highlands, with minor orbit-to-orbit striping. (b) Emissivity at 7.8 μm (Diviner channel 3), computed relative to the Christiansen Feature using the standard CF-fitting procedure. This wavelength is sensitive to compositional and textural differences. Background image: Moon LRO LROC WAC Global Morphology Mosaic 100m, June 2013 (Speyerer et al., 2011; Wagner et al., 2015).

690

2.5 Comparison of the three methods

2.5.1 Temperature

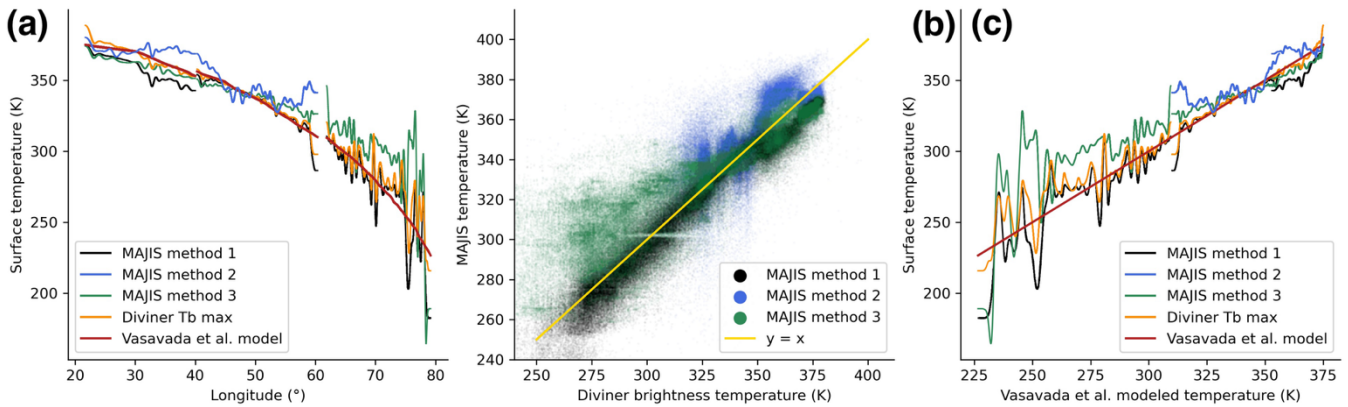
695 The comparison between three independent approaches for estimating lunar surface temperature from MAJIS data reveals systematic differences that depend on solar incidence angle and the radiometric quality of the observations. Figure 13 summarizes the results of (1) Bayesian inversion (Tosi et al., 2014), (2) an empirical correction based on laboratory-derived relationships (Li and Milliken, 2016), and (3) a roughness-informed thermal model (Wohlfarth et al., 2023). ~~The latter approach requires discretizing the observational parameter space into sub-categories of incidence, emission, and roughness to ensure computational feasibility, which leads to the gridded appearance visible in Figure 13b.~~

700 The comparison among the three retrieval approaches highlights systematic differences that depend strongly on solar incidence angle and illumination conditions. The empirical correction following Li and Milliken (2016) increasingly diverges from the Vasavada thermal model at incidence angles beyond $\sim 55^\circ$. This behaviour likely reflects the fact that the correction law was derived from laboratory spectra acquired under fixed geometry ($i = 30^\circ$, $e = 0^\circ$), conditions that differ markedly from the high phase angle ($\sim 90^\circ$) and variable incidence sampled during the JUICE flyby. By contrast, the Bayesian inversion shows greater robustness at high incidence and low-SNR data, producing smoother and more conservative temperature estimates that remain
705 relatively close to the Vasavada curve. However, a notable deviation between Methods 1 and 2 and the Vasavada model is observed in the longitude range $30\text{--}40^\circ$ corresponding to highland terrains observed in C4 under incidence angles in the range $35^\circ\text{--}45^\circ$, where surface roughness and anisothermality introduce systematic biases. ~~The roughness-informed Model 3 (Wohlfarth et al., 2023) can reproduce the expected temperature trends under well-illuminated conditions ($i < 60^\circ$), but in the present implementation its agreement with Diviner and with the Vasavada model is not systematically better than the other
710 approaches and depends on the adoption of the Hapke's model for the reflected component. In fact, this approach may lead to deviations in the derived single-scattering albedo because the photometric treatment becomes more uncertain at phase angle $\sim 90^\circ$. This potential discrepancy may partially propagate into the roughness values retrieved in Section 2.3, which depend directly on the single-scattering albedo, and consequently into the retrieved temperatures. ~~on the discretization of the geometry space used for computational tractability.~~ Nonetheless, in shadowed or high incidence regions, even this approach remains
715 challenged by anisothermality and unresolved sub-pixel topography, which introduce localized deviations.~~

Taken together, these results are an intercomparison of the specific implementations used here, rather than evidence of intrinsic complementarity among the methods. The empirical correction performs best when the observing geometry is close to its laboratory calibration conditions, but it becomes increasingly sensitive to extrapolation at high phase angle and high incidence. The Bayesian inversion is comparatively stable in low-SNR regimes in this study, largely due to the strength of the a priori
720 regularization, which can also damp local variability at intermediate incidence angles. The roughness-informed approach can reduce geometry-driven biases by explicitly representing sub-pixel facet distributions in the forward model; however, its performance in this work is strongly implementation-dependent (e.g., roughness scaling and photometric/albedo

parameterization), and therefore it should be interpreted as a physically motivated sensitivity test rather than a uniformly superior solution.

725 Taken together, the three methods illustrate complementary strengths. The empirical approach is most accurate when illumination conditions resemble those of the laboratory calibration but is prone to error at high incidence. The Bayesian inversion is robust under challenging radiometric conditions, although it may underestimate surface temperatures at intermediate incidence angles, reflecting the strong regularization imposed by the a-priori covariance, which can suppress local spectral gradients. The roughness-informed thermal model achieves the best overall consistency with Diviner and Vasavada, yet still inherits limitations from geometric roughness and phase-angle extremes. The systematic differences among the three approaches underscore the importance of cross-validation and demonstrate that combining them yields the most reliable interpretation of MAJIS-derived lunar surface temperatures across diverse observational geometries and terrains.



735 **Figure 13. Comparison of temperature retrieval methods.** Surface temperature estimates from MAJIS infrared data obtained with three independent approaches: (1) Bayesian inversion following Tosi et al. (2014) (black), (2) empirical correction following Li and Milliken (2016) (blue gray), and (3) a roughness-informed thermal model following Wohlfarth et al. (2023) (green light gray). (a): retrieved temperatures along the JUICE ground track as a function of longitude, compared with Diviner maximum brightness temperatures (orange blue) and the thermophysical model of Vasavada et al. (1999) (red). (b): pixel-by-pixel comparison between MAJIS-derived temperatures and Diviner brightness temperatures, with the one-to-one line in yellow. The discretized appearance of Method 3 in this panel results from its computational design: pixels are grouped into sub-categories on a 3D grid of incidence, emission, and roughness parameters, while assuming a constant average phase angle, to ensure tractable run times. (c): comparison between MAJIS- and Diviner-derived temperatures, and the Vasavada et al. (1999) model. All methods converge within a few kelvins under well illuminated conditions, though larger deviations occur near the terminator.

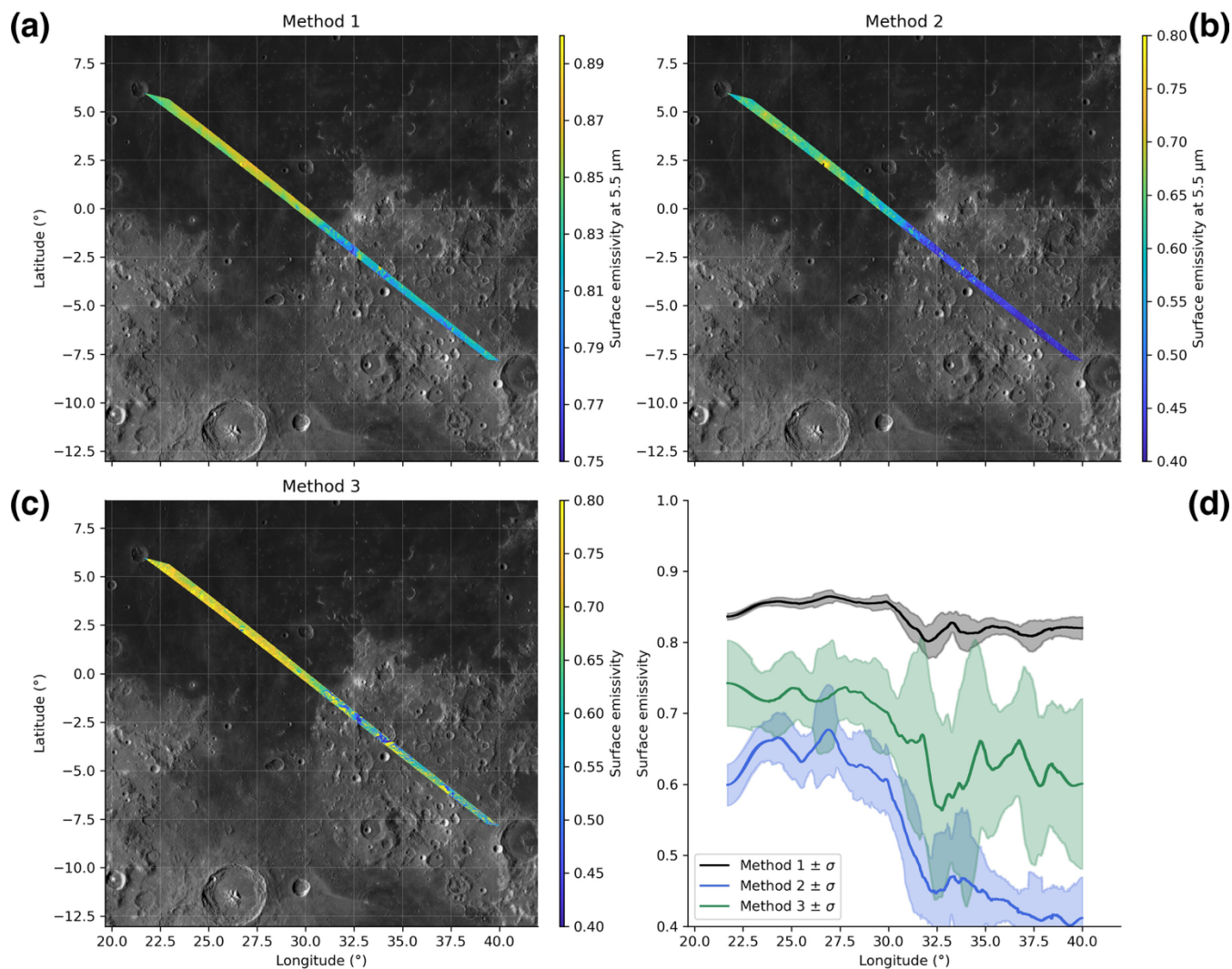
740
745

2.5.2 Emissivity

750 Before comparing emissivity results, we clarify that different retrieval approaches naturally return different emissivity quantities. In Method 1 (Bayesian inversion), emissivity is retrieved as a spectral, channel-by-channel directional emissivity over the thermal window (4.5–5.56 μm), and for map-level comparison we report the value at 5.5 μm . In Method 2 (empirical correction), emissivity at 5.5 μm is inferred from the measured radiance using the approximation $I_{5.5} \approx \varepsilon_{5.5} B_{\lambda}(T)$, assuming that the reflected component is negligible at this wavelength for the considered scenes; the resulting should thus be interpreted as an effective emissivity tied to the adopted temperature estimate and viewing geometry. In Method 3 (roughness-informed model), emissivity is treated as spectrally neutral over 5.0–5.5 μm and retrieved jointly with temperature within a sub-pixel
755 facet formulation; the retrieved parameter represents a grey effective emissivity that absorbs residual directional and sub-pixel effects not explicitly captured by the simplified spectral emissivity assumption. In this section, the intercomparison is therefore restricted to a common observable: an effective directional emissivity at 5.5 μm under the MAJIS observation geometry.

With this definition, Figure 14 compares emissivity estimates from the MAJIS lunar observation C4 that are consistent in wavelength (5.5 μm) and in observational meaning (effective directional emissivity), while differences among methods
760 primarily reflect their distinct modelling assumptions and implementation choices; the comparison is shown both in map view and as longitudinal profiles.

~~Figure 14 presents a comparative analysis of surface emissivity derived from the MAJIS lunar observation C4, which was acquired under the most favourable illumination conditions. This dataset offers the best opportunity to assess emissivity retrievals, given the temperature uncertainties discussed in subsection 2.5.1. Three different approaches are considered: (1) the
765 Bayesian inversion developed by Tosi et al. (2014), constrained by radiative transfer modelling; (2) the empirical thermal correction method derived from Li and Milliken (2016); and (3) a roughness-informed thermal model following Wohlfarth et al. (2023), adapted to the geometry of the JUICE flyby.~~



770 **Figure 14. Comparison of emissivity retrieval methods.** Emissivity estimates for the C4 observation obtained with the Bayesian approach
 or Method 1 (a), the Li and Milliken method or Method 2 (b), and the roughness-informed thermal model or Method 3 (c), respectively.
 Background image: Moon LRO LROC WAC Global Morphology Mosaic 100m, June 2013 (Speyerer et al., 2011; Wagner et al., 2015).
 Panel (d) shows a comparison between the emissivity estimated with Method 1 (black shaded plot dots), Method 2 (blue shaded plot dots)
 and Method 3 (green shaded plot dots) as a function of longitude.

775

~~Figure 14 compares the emissivity retrievals from the three methods in both map view and as longitudinal profiles.~~ Figures
 14a–c present the spatial distribution of emissivity at 5.5 μm derived with the Bayesian inversion (Method 1), the empirical
 correction (Method 2), and the roughness-informed thermal model (Method 3), respectively. In Method 1, full spectral
 emissivity profiles between 4.5 and 5.5 μm are retrieved using a prior of 0.70 ± 0.15 , and only the scalar value at 5.5 μm is
 780 mapped. Method 2 computes emissivity at the same wavelength directly from Kirchhoff's law, assuming negligible reflected

sunlight, whereas Method 3 retrieves emissivity over 5.0–5.5 μm by explicitly including roughness and illumination geometry in the forward radiative transfer. Panel 14d summarizes these results as a function of longitude, allowing direct comparison of terrain-dependent variability among the three approaches.

All methods detect the same first-order geophysical signal: Mare Tranquillitatis exhibits higher emissivity than the surrounding highlands. However, the magnitude and variability of emissivity differ substantially across methods. The Bayesian inversion (black shaded plot blue dots in Figure 14d) yields values tightly clustered around $\varepsilon \approx 0.85$ in the mare and 0.75–0.85 in the highlands with minimal scatter, reflecting the smoothness constraint imposed by the prior covariance. The empirical method (blue shaded plot red dots) produces significantly lower values (0.60–0.70 in the mare and 0.40–0.60 in the highlands) and shows enhanced pixel-to-pixel noise. Method 3 (green shaded plot dots) returns similar values— $\varepsilon \approx 0.60$ –0.70 in the mare and $\varepsilon \approx 0.50$ –0.80 in the highlands—with greater variability in rough or cratered areas. This variability is consistent with the inherently directional nature of emissivity and the influence of surface slopes on thermal emission (e.g., Rozitis and Green, 2011).

Although Methods 2 and 3 both assume spectrally neutral emissivity over their retrieval interval, their behaviour in highland regions differs markedly. Method 3 systematically yields higher emissivity than Method 2, falling between the Bayesian and empirical estimates. This indicates that the underestimation by Method 2 is not solely due to the grey-emissivity assumption, but also to its neglect of roughness (and associated beaming effects), its reliance on laboratory calibration relationships obtained at fixed geometry, and the propagation of uncertainties from the multiple wavelengths used in the correction. By explicitly accounting for geometry and roughness, Method 3 mitigates several of these limitations, even within a narrower spectral range.

The spatial maps further illustrate these differences in retrieval fidelity. The Bayesian-derived map (Figure 14a) shows a smooth and coherent emissivity pattern that closely reflects the large-scale thermophysical contrast between mare and highlands. The empirical map (Figure 14b) displays stronger noise and variability, particularly over highland terrains, while the roughness-informed model (Figure 14c) preserves the large-scale trend and captures localized fluctuations in rough areas and along crater rims, consistent with its explicit sensitivity to surface geometry. Despite their methodological differences, all three approaches reproduce the same first-order emissivity dichotomy between mare and highlands.

This contrast aligns with known compositional and textural differences. Feldspathic highland regoliths are more porous and finely comminuted, enhancing multiple scattering and lowering effective emissivity, whereas denser, smoother basaltic mare surfaces exhibit higher emissivity (e.g., Donaldson Hanna et al., 2012). This interpretation is consistent with full-disk observations from NOAA/HIRS (3.75–15 μm) analysed by Müller et al. (2021), who reported systematically lower emissivity over highlands—particularly beyond 5 μm —and attributed this to variations in composition, grain size, and roughness. The agreement between MAJIS-derived emissivity and independent long-wavelength datasets provides supporting evidence for the observed mare-highland dichotomy and underscores the value of combining multiple retrieval strategies to isolate instrumental, geometric, and geophysical effects. Additional context in the 3–4 μm domain is provided by disk-resolved mid-infrared observations from the geostationary Gaofen-4 (GF-4) satellite. Wu et al. (2021) imaged the full lunar disk in the MIR

815 band 6 (3.50–4.10 μm ; effective wavelength \sim 3.77–3.82 μm depending on the relative reflected/thermal contribution). Their
analysis highlights that, at these wavelengths, the measured radiance is governed by the interplay of reflected sunlight and
thermal emission, and that maria can appear brighter than highlands under warm conditions due to enhanced thermal emission
from low-albedo basalts. While GF-4 does not provide hyperspectral emissivity retrievals, it independently confirms that the
3–5 μm region is a crossover regime in which temperature–emissivity coupling and illumination geometry strongly affect
820 inferred surface properties.

Complementary context at longer wavelengths is provided by Lucy/L’TES, which acquired hyperspectral thermal-infrared
lunar spectra in the range 5.8–100 μm during the 2022 Earth gravity assist and derived emissivity spectra consistent with
Diviner Christiansen-feature constraints and Apollo soil laboratory measurements (Christensen et al., 2025). This TIR
benchmark anchors the interpretation of the Diviner comparison below, emphasizing that mare–highland emissivity ordering
825 depends on wavelength and bandpass across the CF-related spectral structure.

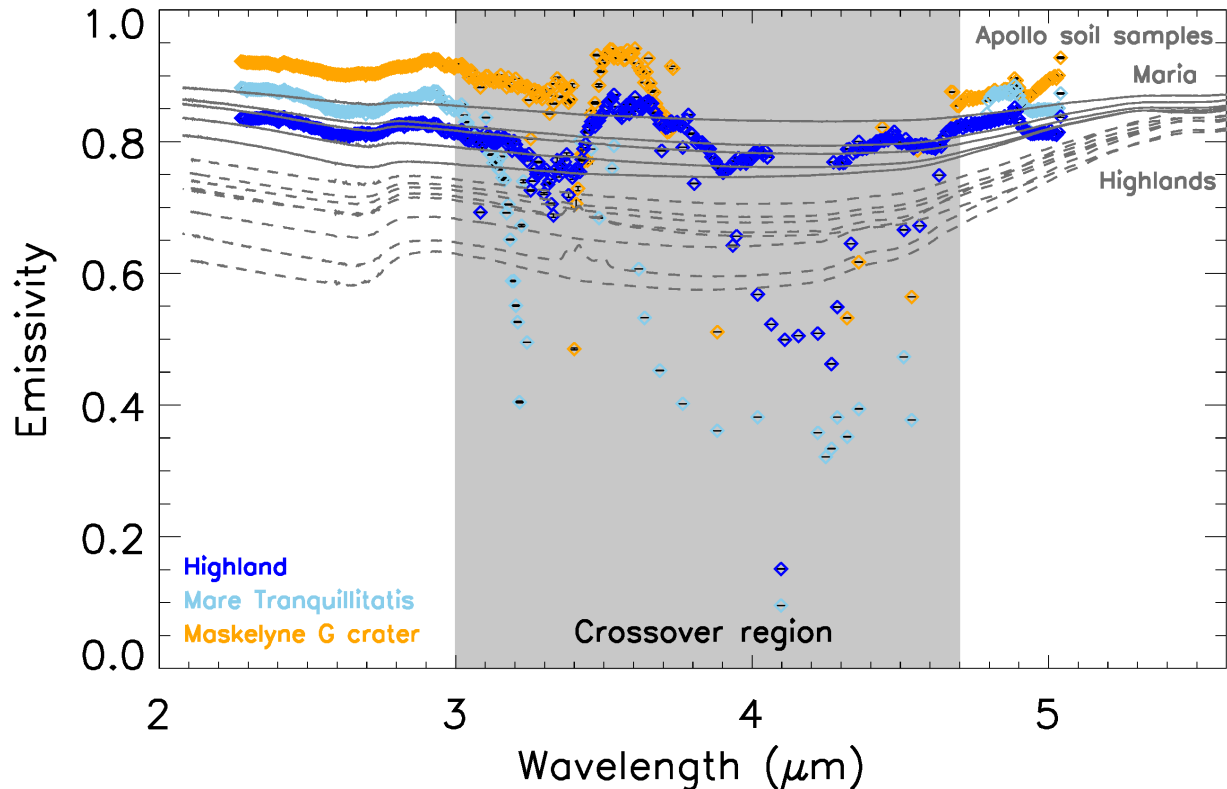
When compared with Diviner, a clear bandpass dependence emerges. The Diviner emissivity product discussed here is derived
for channel 3 (7.8 μm), i.e. on the short-wavelength side of the Christiansen Feature (CF) for feldspathic highland materials
(e.g., Greenhagen et al., 2010). Because mare basalts typically exhibit CF positions at longer wavelengths than feldspathic
terrains, the emissivity measured in Diviner channel 3 can therefore be higher over highlands than over maria at this specific
830 wavelength (see Figure 11b in Ren et al., 2021), even though the relative ordering may differ at shorter wavelengths.
Accordingly, the Diviner channel-3 comparison should be interpreted as a narrow-band diagnostic linked to CF position and
composition, rather than as evidence that highlands are generally more emissive than maria across the mid-infrared.

In the MAJIS range (\leq 5.56 μm), our emissivity estimates indicate higher values over mare basalts than over surrounding
highlands, consistent with independent measurements in the 3–5 μm region (e.g., Chandrayaan-2/IIRS; Ojha et al., 2024) and
835 with published laboratory spectra showing that emissivity contrasts can vary with wavelength and composition. The
comparison with Diviner thus provides complementary context across wavelength regimes: MAJIS samples the short-
wavelength side of the CF and the crossover region between reflected and emitted radiance, whereas Diviner channel 3 samples
the CF flank near 7.8 μm . This combined view highlights the need to interpret emissivity in terms of wavelength-dependent,
bandpass-specific quantities rather than a single “bulk” emissivity, especially when comparing instruments that sample
840 different parts of the CF-related spectral structure.

~~When compared with Diviner, a clear wavelength dependence emerges. Diviner channel 3 radiances and emissivity (7.8 μm)
show the opposite trend—highlands appearing more emissive than maria—consistent with the analysis of Ren et al. (2021)
and reflecting the well-established inversion across the Christiansen Feature. This behaviour is fully supported by laboratory
spectra of lunar soils and analogues, which show that feldspathic materials become relatively more emissive beyond 7–8 μm ,
845 whereas basaltic surfaces dominate at shorter wavelengths. Retrievals from Chandrayaan-2/IIRS in the 3–5 μm range (Ojha et
al., 2024) similarly report emissivity values between 0.60 and 0.80 with pronounced spatial variability at shorter wavelengths,
reinforcing the wavelength-dependent behaviour observed by MAJIS.~~

850 Together, these datasets indicate that highlands exhibit lower emissivity than maria up to $\sim 5.5 \mu\text{m}$ —the upper limit of MAJIS sensitivity—while beyond this wavelength the trend reverses. This spectral crossover, governed by the vibrational properties of silicate minerals and by particle-scale roughness, reconciles the MAJIS and Diviner observations and highlights their complementarity.

The CF positions derived from Diviner additionally provide an independent compositional indicator that complements MAJIS hyperspectral retrievals at shorter wavelengths, reinforcing the distinction between mare basalts and feldspathic highlands. ~~The comparison thus demonstrates the synergy between the two instruments:~~ In practice, Diviner offers long-wavelength, global coverage with excellent diurnal sampling, while MAJIS provides high-resolution hyperspectral measurements in the 3.0–5.56 μm range, bridging the gap between near- and mid-infrared observations. Taken as a whole together, these datasets support ~~underscore~~ the wavelength-dependent nature of lunar emissivity and the importance of multi-instrument analyses for disentangling the combined effects of composition, texture, roughness and thermal environment on airless-body surfaces.



860

Figure 15. Spectral emissivity of different terrains. Spectral emissivity profiles for three lunar surface units retrieved with the Bayesian inversion applied to MAJIS C4 data. The thermal retrieval is performed over the 3.0–5.56 μm interval, and the resulting emissivity is reported

865 here as spectral directional emissivity under the opaque-surface assumption. For wavelengths shorter than 3.0 μm , emissivity is extended using the photometrically corrected reflectance via Kirchhoff's relation $\epsilon_d(\lambda)=1-r_{\text{hd}}(\lambda)$. Shown are terrain-averaged emissivity profiles for a highland region (blue), Mare Tranquillitatis (cyan), and the Maskelyne G crater (orange). For qualitative laboratory context, emissivity spectra of Apollo soil samples are overplotted in grey, with representative mare and highland sample groups indicated with solid and dashed lines, respectively. Formal uncertainties on the MAJIS emissivity averages are very small and are shown as black markers. The shaded region marks the 3.0–4.7 μm crossover interval, where reflected and emitted contributions are comparable and emissivity retrievals are most sensitive to modelling assumptions and residual calibration effects.

870

~~Spectral emissivity profiles retrieved from three lunar surface units using the Bayesian inversion applied to MAJIS data C4. The thermal retrieval is performed only over the 3.0–5.56 μm range, where the signal is dominated by emitted radiance. The resulting emissivity values are then extended to the full 2.0–5.56 μm interval by combining the retrieved emissivities with the photometrically corrected reflectance ($\epsilon = 1 - r$). Shown are average emissivity profiles for a highland region (blue), Mare Tranquillitatis (green), and the Maskelyne G crater (red). Highland terrain displays the lowest emissivity, mare surfaces slightly higher values, and the crater the highest, consistent with blockier and less weathered material. Error bars (formal uncertainties) are very small and appear as black markers. The grey box highlights the “crossover region” (3.0–4.7 μm) where reflected sunlight and thermal emission are comparable.~~

875

Building on this result, Figure 15 presents representative spectral emissivity profiles extracted from three distinct lunar terrains: highlands, Mare Tranquillitatis, and Maskelyne G, a 6-km fresh crater located within the mare. These profiles reveal clear, systematic differences that reflect underlying variations in composition and surface texture, grain size, and thermophysical properties. The spectra were derived using the Bayesian inversion method applied to MAJIS data in the 3.0–5.5 μm range, under the assumption of an emissivity prior of 0.70 ± 0.15 and no photometric correction. Across the spectral interval, the highland spectrum shows the lowest emissivity values, typically between 0.78 and 0.85, consistent with the known properties of feldspathic materials. Mare Tranquillitatis exhibits higher emissivity across the same wavelengths, indicative of denser, basaltic composition and surface texture differences surfaces with reduced porosity and higher thermal inertia. The Maskelyne G crater spectrum displays the highest emissivity, close to or above 0.90 throughout the thermal domain, consistent with exposure of coarser, less-weathered or blocky material exhibiting reduced multiple scattering and enhanced thermal emission (Salisbury et al., 1987; Mustard and Hays, 1997; Donaldson Hanna et al., 2012), and potentially enhanced by localized self-heating and thermal-infrared beaming within concave or rough crater interiors (Rozitis and Green, 2011; Davidsson and Rickman, 2014). Mineralogical analysis of the same MAJIS dataset indicates that this crater is compositionally distinct from the surrounding terrain, showing an enhanced abundance of pyroxene-rich material, possibly pigeonite (Zambon et al., this issue).

880

885

890

While the emissivity differences between terrains are geologically meaningful, the presence of apparent absorption-like minima—particularly between 3.0 and 4.7 μm —requires careful interpretation. These features are not associated with known silicate vibrational bands, which typically occur beyond 8 μm , outside the MAJIS spectral range. Instead, they likely result from challenges in retrieving emissivity in the transition region where reflected solar and thermally emitted radiation overlap.

895

In this “crossover region,” small errors in radiometric calibration, assumed surface reflectance, or modelling of solar contribution can propagate into the retrieval, leading to artificial depressions in emissivity. To assess whether the $\sim 3.5 \mu\text{m}$ structure reflects a systematic signal in the measurements, we inspected the C4 data in radiance space, excluding the first 17 slit samples that were intentionally omitted from the thermal analysis because of the straylight test configuration. No scene-wide absorption centred at $\sim 3.5 \mu\text{m}$ is found in the median radiance spectrum. The corresponding channel shows only modest sample-dependent residuals, generally within a few percent across the usable slit region. We therefore do not regard the $\sim 3.5 \mu\text{m}$ structure as a robust scene-wide spectral feature in the radiance data. For additional context, in Figure 15 we also compared the MAJIS spectral profiles of retrieved emissivity with laboratory emissivity spectra (calculated as $1 - \text{reflectance}$) of Apollo soil samples available in the ECOSTRESS database (<https://speclib.jpl.nasa.gov/library>). The comparison should be interpreted qualitatively, because the MAJIS retrieval yields an effective directional emissivity under the JUICE flyby geometry, whereas the Apollo spectra represent laboratory emissivity measured under controlled conditions. Within the MAJIS retrieval window ($3.0\text{--}5.56 \mu\text{m}$), Figure 15 primarily demonstrates a reproducible relative offset among the terrain-averaged emissivity curves extracted from the selected highland, mare, and fresh-crater regions. In the thermally dominated part of the spectrum, mare basalts and Maskelyne G exhibit systematically higher retrieved emissivity than the surrounding highlands, consistent with the first-order mare–highland contrast observed in the emissivity maps (Figure 14) and with the expected wavelength dependence of lunar emissivity. A weak qualitative similarity can be noted in the $2.5\text{--}2.8 \mu\text{m}$ range, where the MAJIS-derived emissivity profiles display a relative variation broadly comparable to that observed in the Apollo soil spectra. However, this comparison remains only indicative, since emissivity in this interval is derived from reflectance rather than directly retrieved from the thermally dominated part of the spectrum. On the other hand, the $3.0\text{--}4.7 \mu\text{m}$ crossover interval is ill-conditioned for reflected/thermal separation, so the relative ordering of terrain-averaged emissivities near $\sim 4 \mu\text{m}$ may be affected by retrieval/calibration residuals; we therefore emphasize the thermally dominated part of the MAJIS window for geophysical interpretation.

~~The variability in shape and depth of these minima across different terrains further supports their non-mineralogical origin. Although future improvements in reflectance modelling may mitigate these effects, under the current assumptions such features should be regarded as retrieval artefacts rather than true diagnostic absorption bands. These results confirm that spectral emissivity in the $3\text{--}5 \mu\text{m}$ region—though shortward of the Christiansen feature classic Reststrahlen bands—encodes valuable information about lunar surface properties. The clear separation between the emissivity profiles retrieved from the three terrains underscores the potential of MAJIS for identifying subtle differences in surface roughness, texture, and thermal behaviour, particularly when integrated with high-resolution geological context and cross-wavelength validation from instruments such as Diviner.~~

3 Conclusions

930 The MAJIS observations obtained during the JUICE lunar flyby provide an appealing opportunity to assess the thermal and emissivity properties of the Moon at high spatial and spectral resolution. By applying three independent approaches—Bayesian inversion (Tosi et al., 2014), empirical correction following Li and Milliken (2016), and a roughness-informed thermal model following Wohlfarth et al. (2023)—we derived surface temperatures and emissivity values that can be cross-validated against one another and compared with both Diviner datasets and thermophysical models. These methodological differences are also relevant for reflectance-based analyses around 3 μm , where residual thermal emission can bias inferred band strengths.

935 Although this study does not perform a dedicated lunar hydration analysis, the thermal-removal problem addressed here is directly relevant to the interpretation of possible absorptions around 3 μm . Companion work by Langevin et al. (this issue) reports a weak, broad structure near $\sim 2.9 \mu\text{m}$ in MAJIS radiance spectra acquired at mid-to-high incidence, but explicitly cautions that its interpretation is limited because this spectral interval coincides with the LVF–interface spectral gap—also discussed by Zambon et al. (this issue)—and because reflectance band-strength estimates in this region are highly sensitive to
940 the model-dependent subtraction of the thermal contribution in the reflected/thermal crossover regime.

The comparison among methods highlights both convergence and divergence. All three techniques reproduce the expected temperature increase with solar illumination, with agreement within a few kelvins in the most favourable radiometric conditions (C3–C4). However, their behaviour diverges at higher incidence angles or in low-SNR scenes. The empirical approach, being tied to laboratory-derived correction laws, tends to overestimate surface temperatures under geometries far
945 from its calibration range, particularly at $i > 55^\circ$, where the relative contribution of reflected radiance increases and the temperature–emissivity separation becomes more degenerate. The Bayesian approach, by contrast, remains more stable under these conditions but shows a tendency to underestimate peak temperatures at intermediate incidence angles, a likely manifestation of over-regularization. The roughness-informed thermal model can reduce geometry-driven biases by representing sub-pixel facet distributions in the forward model, but its agreement with Diviner/Vasavada in this study remains
950 implementation-dependent and varies across scenes (e.g., assumptions on roughness scaling, albedo).

A central result of this study is the characterization of bandpass-specific emissivity contrasts across major lunar terrains within the MAJIS thermal range ($\leq 5.56 \mu\text{m}$). Despite methodological differences, the three approaches consistently retrieve higher effective emissivity over Mare Tranquillitatis than over the surrounding feldspathic highlands, with locally enhanced values over fresh crater interiors such as Maskelyne G. This contrast is consistent with established compositional and textural
955 differences between basaltic and feldspathic units (e.g., varying mafic mineral content and space-weathering state), and with geometry-dependent effects linked to surface roughness. While micro-texture (including porosity and packing state) may contribute to effective emissivity, the present daytime flyby data do not provide independent constraints on thermal inertia or thermal conductivity; we therefore restrict the interpretation to emissivity contrasts inferred in the MAJIS bandpass under the observed geometries.

960 The comparison with Diviner is used here to provide cross-wavelength context rather than a direct emissivity equivalence. Diviner channel-3 emissivity at 7.8 μm samples the short-wavelength flank of the Christiansen Feature for feldspathic materials; because mare CF positions occur at longer wavelengths, highlands can appear more emissive than maria at this specific wavelength. This behaviour is therefore interpreted as a narrow-band effect controlled by CF position and composition, not as evidence that highlands are generally more emissive than maria across the mid-infrared. In combination, MAJIS (≤ 5.56 965 μm) and Diviner (7.8 μm) emphasize that emissivity must be interpreted as a wavelength-dependent, bandpass-specific quantity when comparing instruments sampling different parts of the CF-related spectral structure.

Independent measurements in adjacent mid-infrared regimes further support the need for a bandpass-specific interpretation of lunar radiance and emissivity. Gaofen-4 acquired disk-resolved images of the Moon in a 3.50–4.10 μm band (effective wavelength ~ 3.8 μm), showing that the mid-infrared lunar appearance is governed by the combined contribution of reflected 970 sunlight and thermal emission, with maria becoming brighter than highlands under conditions where thermal emission dominates and with the brightness distribution evolving with illumination geometry (Wu et al., 2021). At longer wavelengths, Lucy/L’TES provided well-calibrated hyperspectral thermal-infrared (TIR) lunar spectra and retrieved an emissivity spectrum with a Christiansen-feature maximum near 8.15 μm that agrees with Diviner CF constraints and Apollo soil laboratory spectra (Christensen et al., 2025). Together, these complementary datasets emphasize that apparent mare–highland emissivity ordering 975 can change with wavelength across the CF-related spectral structure, and that cross-instrument comparisons must be framed in terms of the specific bandpasses and observation geometries involved.

The roughness-informed thermal model adds an important dimension by explicitly accounting for sub-pixel temperature variability (i.e., mixtures of sunlit and shadowed facets with different slopes within one pixel). This helps interpret deviations observed at high incidence angles and over rugged terrains, where unresolved slopes and shadowing can bias temperature 980 retrievals based on simplified radiative balance assumptions. In the present implementations, the empirical method is most sensitive to these effects because it assumes a fixed-geometry correction law, whereas the Bayesian approach may damp such variability through regularization. By incorporating roughness-driven facet distributions within an energy-balance framework, the roughness-informed model mitigates some of these biases, although localized deviations remain in the most extreme geometries and/or lowest-SNR conditions.

985 The thermophysical patterns retrieved by MAJIS show a clear correspondence with the mineralogical variability independently identified in the VNIR domain (Zambon et al., this issue). In Mare Tranquillitatis, areas exhibiting deep 1–2 μm pyroxene absorptions—indicative of Fe- and Ca-rich basalts—tend to coincide with higher effective emissivity and warmer daytime temperatures, consistent with compositional differences (mafic vs feldspathic units) and with variations in surface maturity. In contrast, feldspathic highlands, spectrally dominated by plagioclase and characterized by strong space-weathering reddening, 990 show lower emissivity and more heterogeneous thermal behaviour. Local thermal enhancements near fresh craters similarly match VNIR detections of compositionally fresher, blocky pyroxene-rich materials. These correlations indicate that the 3–5.5 μm radiance field and the corresponding effective emissivity products are modulated by composition and surface maturity, in addition to illumination geometry and unresolved roughness.

995 Taken together, the MAJIS observations demonstrate that the instrument provides precise formal uncertainties under favourable conditions and that physically motivated retrieval strategies can reproduce the main daytime thermal patterns and bandpass-specific emissivity contrasts at MAJIS resolution. The combined analysis indicates that variations in composition, surface maturity, and unresolved roughness/illumination geometry jointly modulate the retrieved temperature and effective emissivity fields, while limitations remain in the crossover interval where reflected and emitted components are comparable. These results provide a consistent framework for interpreting MAJIS mid-infrared radiances over well-characterised lunar terrains and for identifying observational regimes in which model assumptions dominate the solution. The lunar dataset therefore serves as a physically constrained test case in the mid-infrared crossover region, and the present work should be understood as a methodological and scientific consistency assessment of MAJIS thermal retrieval strategies. While the instrument-level validation is addressed elsewhere, this work demonstrates that physically motivated inversion schemes can reproduce lunar radiances in the mid-infrared crossover region without introducing inconsistencies with established lunar properties. The specific thermophysical parameters differ between our Moon and the Galilean moons. However, the inversion strategy and modelling approach developed in this work form a transferable methodological basis for the interpretation of future MAJIS observations of icy surfaces such as Callisto, where subsolar temperatures are predicted to produce a detectable thermal signal within the MAJIS spectral range (Royer et al., 2025), supporting potential future applications.

1010 ~~The MAJIS observations obtained during the JUICE lunar flyby provide a unique opportunity to assess the thermal and emissivity properties of the Moon at high spatial and spectral resolution. By applying three independent approaches—Bayesian inversion (Tosi et al., 2014), empirical correction following Li and Milliken (2016), and a roughness-informed thermal model following Wohlfarth et al. (2023)—we derived surface temperatures and emissivity values that can be cross-validated against one another and compared with both Diviner datasets and thermophysical models.~~

1015 ~~The comparison among methods highlights both convergence and divergence. All three techniques reproduce the expected temperature increase with solar illumination, with agreement within a few kelvins in the most favourable radiometric conditions (C3–C4). However, their behaviour diverges at higher incidence angles or in low-SNR scenes. The empirical approach, being tied to laboratory-derived correction laws, tends to overestimate surface temperatures under geometries far from its calibration range, particularly at $i > 55^\circ$, where reflected and thermal contributions overlap, and noise levels rise. The Bayesian approach, by contrast, remains more stable under these conditions but shows a tendency to underestimate peak temperatures at intermediate incidence angles, a likely manifestation of over-regularization. The roughness-informed thermal model provides the closest match to Diviner brightness temperatures and to the Vasavada et al. (1999, 2012) thermophysical model under well-lit conditions, though it is not immune to deviations in shadowed or anisothermal regions. These results indicate that each approach has domain-specific strengths and that their joint application enhances the robustness of the thermal interpretation.~~

1025 ~~A key outcome of this study is the characterization of emissivity across different lunar terrains. Despite methodological differences, all approaches converge on the finding that mare basalts exhibit higher emissivity than surrounding highlands.~~

This contrast is physically meaningful: feldspathic highland regolith is more porous and finely comminuted, which enhances multiple scattering and reduces effective emissivity, while maria, dominated by denser basaltic materials, display higher thermal inertia and higher emissivity. Fresh crater interiors in Mare Tranquillitatis, such as Maskelyne G, reveal even higher emissivity, pointing to blockier and less weathered material with reduced porosity and enhanced conductivity.

The comparison with Diviner further refines this picture. At the shorter side of the Christiansen Feature sampled by MAJIS (3.0–5.5 μm), maria are more emissive than highlands, while at 7.8 μm (Diviner channel 3) the pattern reverses, with highlands appearing more emissive than maria. Laboratory data confirm that such inversions are characteristic of silicate regoliths: feldspathic materials exhibit relatively higher emissivity near the CF, while basalts dominate at shorter wavelengths. This spectral dependence reconciles the apparent contradiction between MAJIS and Diviner and underscores the importance of considering wavelength-dependent emissivity when interpreting lunar surface properties.

The roughness-informed thermal model adds a critical dimension to this analysis by retrieving roughness maps alongside temperature. These maps show enhanced roughness in highland terrains and around crater rims, while mare surfaces appear smoother on average. Such spatial patterns are consistent with the emissivity contrasts described above and with expectations from lunar geology. Importantly, roughness is not merely a static property but a factor that drives anisothermality: rough surfaces contain a distribution of slopes and facets that experience different solar illumination, producing sub-pixel temperature variations. These anisothermal conditions explain, at least in part, the divergence observed between the Bayesian and empirical methods in highland terrains observed under moderated solar illumination. The empirical method, which assumes a simplified radiative balance, fails to account for this complexity and in some cases may tend to overestimate surface temperatures. On the other hand, the Bayesian approach, with its strong regularization, may tend to suppress the thermal variability introduced by anisothermality, leading to underestimation of temperatures. The roughness-informed thermal model, by explicitly incorporating roughness into its energy balance framework, mitigates these effects more effectively, though localized deviations remain in the most extreme geometries.

The thermophysical patterns retrieved by MAJIS show a clear correspondence with the mineralogical variability independently identified in the VNIR domain (Zambon et al., this issue). In Mare Tranquillitatis, areas exhibiting deep 1–2 μm pyroxene absorptions—indicative of Fe- and Ca-rich basalts—display higher emissivity and warmer daytime temperatures, consistent with denser and less weathered regolith. In contrast, the feldspathic highlands, spectrally dominated by plagioclase and characterized by strong space weathering reddening, show lower emissivity and more heterogeneous thermal behaviour. Local thermal enhancements near fresh craters similarly match VNIR detections of compositionally fresh, blocky pyroxene-rich materials. These correlations indicate that the 3–5.5 μm emissivity signal is strongly influenced by composition and regolith maturity, in addition to illumination geometry and surface roughness.

Taken together, the MAJIS observations demonstrate that the instrument retrieves surface temperatures with high precision while also capturing regolith properties that control emissivity and roughness. The emissivity contrasts between maria and highlands, the spectral inversion across the Christiansen Feature, and the explicit roughness estimates collectively reveal a

thermophysical diversity closely linked to composition, grain size, and texture. These results show how the mineralogical variability observed across the lunar surface translates into distinct thermophysical behaviours.

1065 In this context, MAJIS provides a bridge between compositional and physical interpretations of the lunar regolith. By coupling hyperspectral temperature and emissivity modelling, this dataset allows us to explore how mineralogy, grain size and roughness jointly shape the thermal environment of the lunar surface. The synergy between MAJIS and Diviner further demonstrates the value of combining datasets across different spectral ranges. Together, they provide a multi-wavelength view of the Moon that is essential for constraining regolith properties, improving thermophysical models, and guiding the interpretation of thermal emission from other airless bodies.

1070 This end-to-end pipeline, validated by multi-mission heritage, delivers a unique hyperspectral thermal dataset of the Moon. Acquired at a high phase angle and with broad spectral coverage, it provides a critical benchmark for thermal retrieval methods. The successful disentanglement of temperature and emissivity under these conditions establishes a robust framework for MAJIS's exploration of the Jovian system. This capability will be pivotal for probing the thermophysical properties of the most promising targets, such as Callisto, where subsolar temperatures are predicted to produce a detectable thermal signal within the MAJIS spectral range (Royer et al., 2025), thereby extending the instrument's role from compositional mapping to direct thermophysical characterization.

1075

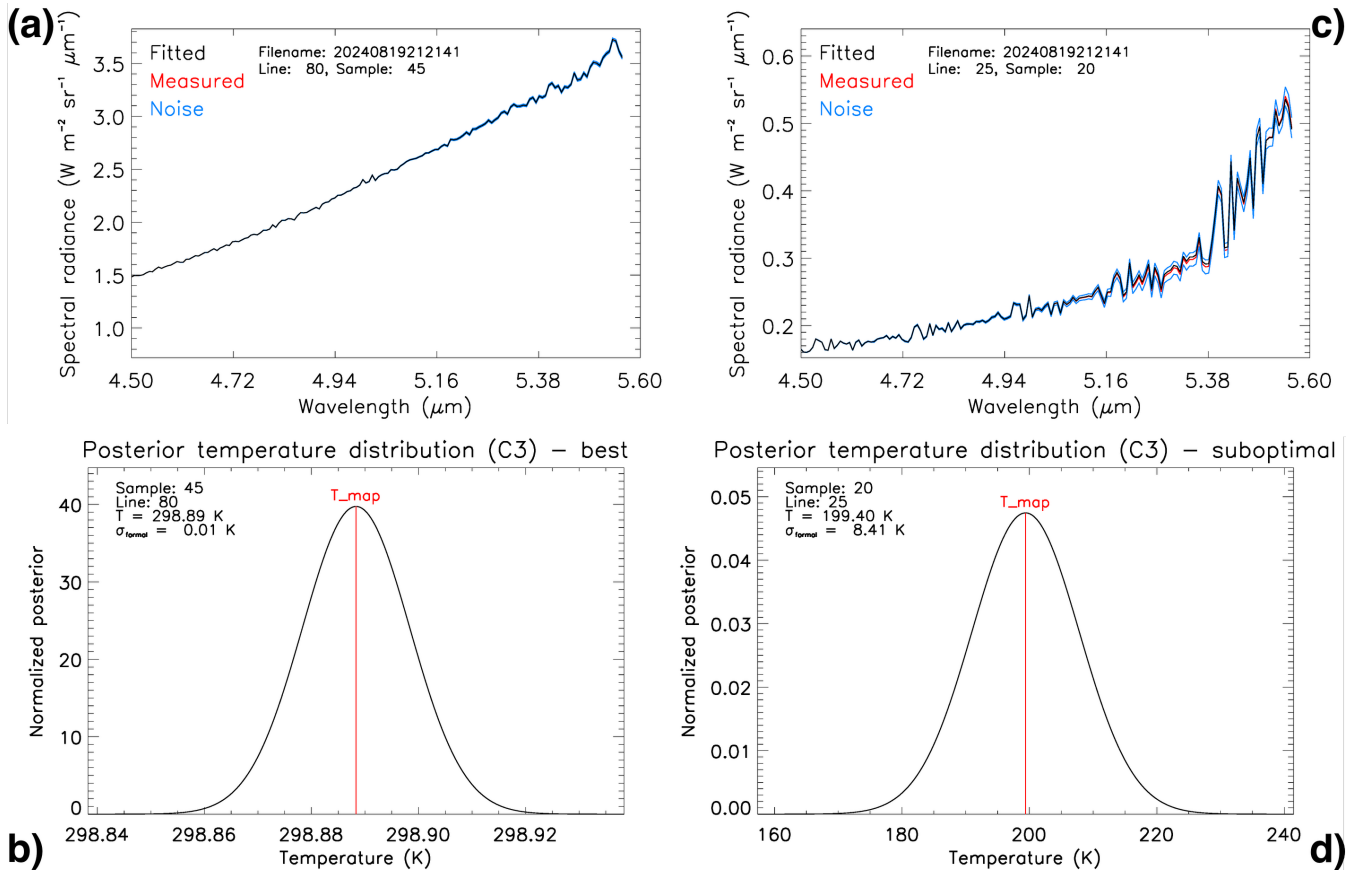
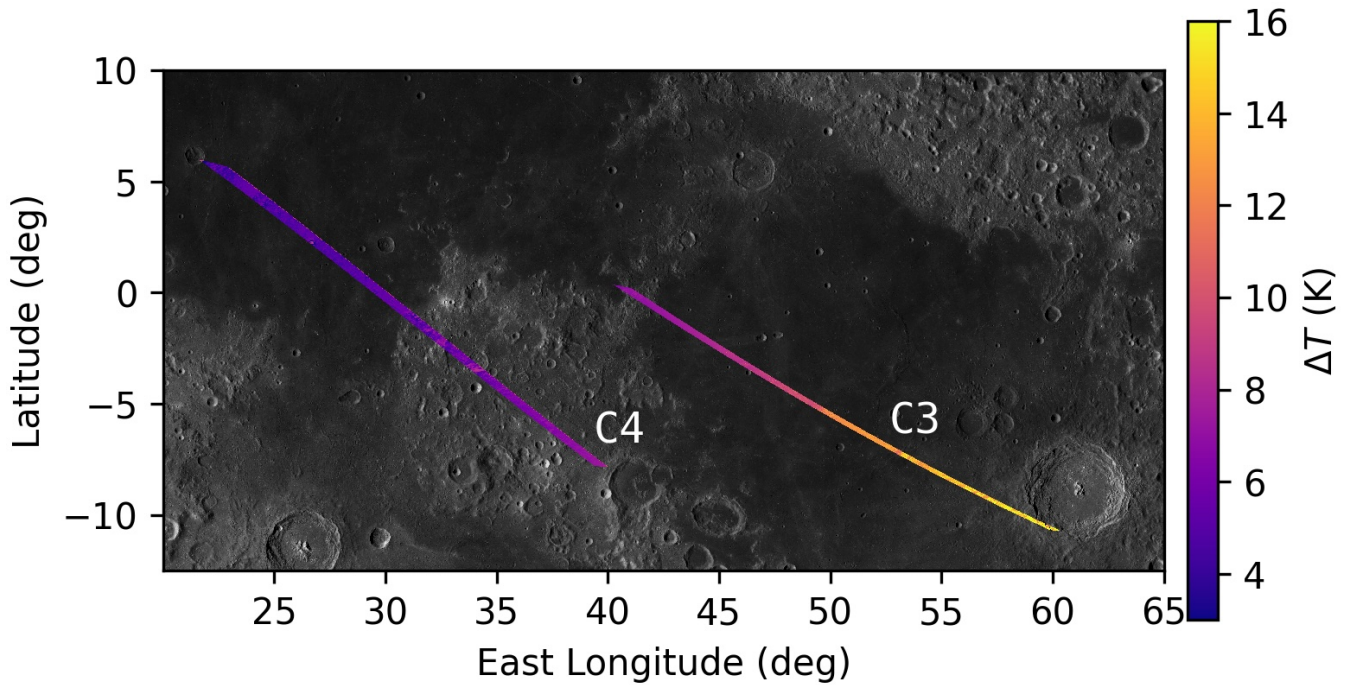


Figure A1. Example MAJIS thermal retrievals and associated posterior temperature distributions (C3). (a) Radiance fit for a best-case pixel (sample = 45, line = 80) from the MAJIS C3 observation (file 20240819212141), retrieved over 4.5–5.5 μm assuming an initial emissivity prior $\epsilon_0 = 0.7$. The measured spectrum (red) is largely overlain by the model fit (black). The Noise Equivalent Spectral Radiance (NESR, light blue) is shown but is difficult to discern at this scale. (b) Corresponding posterior probability density of surface temperature, approximated as a Gaussian centred at the maximum a posteriori estimate T_{map} (red vertical line) with width given by the formal 1-sigma uncertainty from the posterior covariance matrix. (c) Same as (a) for a suboptimal pixel (sample = 20, line = 25), characterized by lower radiance levels and larger relative noise. (d) Corresponding temperature posterior for the suboptimal pixel, showing a broader distribution consistent with the larger formal uncertainty.



1090

Figure A2. Temperature sensitivity to sub-pixel roughness assumptions (C3–C4). Temperature differences obtained when assuming sub-pixel roughness values retrieved in Table 2 compared with the assumption that the macroscopic roughness derived from LRO/LOLA measurements at meter scale represents the sub-pixel roughness. Differences remain small (mostly <5 K) for C4, consistent with the favourable illumination conditions. For C3, the temperature difference increases with increasing longitude and solar incidence angle (Figure 11), in agreement with previous studies (e.g., Bandfield et al., 2015; Wohlfarth et al., 2023).

1095

Table A1. Summary of the temperature values obtained by applying the Bayesian approach to the four data acquired by MAJIS, using the 4.5–5.56 μm range and applying no photometric correction. The different columns specify the a priori hypotheses on the initial emissivity (ϵ_0) along with maximum associated standard deviation. For each MAJIS data, the following information is reported: mean temperature value, mean formal uncertainty associated with the data, 1-sigma dispersion of the data, and maximum temperature value. Units are kelvin.

1100

Observation	Parameter	$\epsilon_0 = 0.7 \pm 0.15$	$\epsilon_0 = 0.8 \pm 0.20$	$\epsilon_0 = 0.9 \pm 0.10$	$\epsilon_0 = 0.95 \pm 0.05$
C1	T_mean	175.7	184.0	184.3	183.3
	σ_{formal}	22.5	23.1	21.3	19.5
	σ_{data}	48.5	32.5	34.6	37.6
	T_max	305.6	299.1	295.6	294.1
C2	T_mean	267.8	270.0	269.4	269.2
	σ_{formal}	3.0	3.2	2.5	1.8
	σ_{data}	49.0	39.2	40.8	41.7
	T_max	345.2	339.9	335.4	333.4

C3	T_mean	333.4	329.2	325.7	324.2
	σ_{formal}	0.8	0.4	0.4	0.2
	σ_{data}	16.1	14.6	13.4	12.8
	T_max	369.8	363.3	357.8	365.4
C4	T_mean	355.9	350.1	345.2	343.0
	σ_{formal}	1.4	1.5	0.7	0.3
	σ_{data}	9.6	9.1	8.7	8.5
	T_max	379.0	372.1	366.3	363.7

Table A2. Summary of the temperature values obtained by applying the Bayesian approach to the four data acquired by MAJIS, using the 3.0–5.56 μm range and applying no photometric correction. The different columns specify the a priori hypotheses on the initial emissivity (ϵ_0) along with maximum associated standard deviation. For each MAJIS data, the following information is reported: mean temperature value, mean formal uncertainty associated with the data, 1-sigma dispersion of the data, and maximum temperature value. Units are kelvin.

Observation	Parameter	$\epsilon_0 = 0.7 \pm 0.15$	$\epsilon_0 = 0.8 \pm 0.20$	$\epsilon_0 = 0.9 \pm 0.10$	$\epsilon_0 = 0.95 \pm 0.05$
C1	T_mean	176.3	183.6	180.2	183.3
	σ_{formal}	22.6	23.3	19.6	19.5
	σ_{data}	47.5	32.9	39.7	37.6
	T_max	301.6	298.5	293.6	294.2
C2	T_mean	267.2	269.8	269.6	269.4
	σ_{formal}	2.9	3.2	2.5	1.8
	σ_{data}	48.8	39.3	40.9	42.1
	T_max	340.1	405.2	340.1	340.1
C3	T_mean	328.0	328.0	328.0	328.0
	σ_{formal}	0.0	0.0	0.0	0.0
	σ_{data}	14.7	14.3	14.2	14.2
	T_max	362.3	430.9	365.6	365.7
C4	T_mean	348.6	348.6	348.6	348.6
	σ_{formal}	0.0	0.0	0.0	0.0
	σ_{data}	8.9	9.0	9.0	9.0
	T_max	383.1	399.3	382.0	378.8

1110 **Table A3.** Summary of the temperature values obtained by applying the Bayesian approach to the four data acquired by MAJIS, using the 3.0–5.56 μm range and applying the Lommel–Seeliger photometric correction. The different columns specify the a priori hypotheses on the initial emissivity (ϵ_0) along with maximum associated standard deviation. For each MAJIS data, the following information is reported: mean temperature value, mean formal uncertainty associated with the data, 1-sigma dispersion of the data, and maximum temperature value. Units are kelvin.

Observation	Parameter	$\epsilon_0 = 0.7 \pm 0.15$	$\epsilon_0 = 0.8 \pm 0.20$	$\epsilon_0 = 0.9 \pm 0.10$	$\epsilon_0 = 0.95 \pm 0.05$
C1	T_mean	176.3	183.6	184.2	183.3
	σ_{formal}	22.6	23.3	21.4	19.5
	σ_{data}	47.5	32.9	34.6	37.6
	T_max	301.6	298.5	295.6	294.2
C2	T_mean	267.2	269.8	269.6	269.4
	σ_{formal}	2.9	3.2	2.5	1.8
	σ_{data}	48.8	39.3	40.9	42.1
	T_max	340.1	405.2	340.1	340.1
C3	T_mean	328.0	328.0	328.0	328.0
	σ_{formal}	0.0	0.0	0.0	0.0
	σ_{data}	14.7	14.3	14.2	14.2
	T_max	362.3	430.9	365.6	365.7
C4	T_mean	348.6	348.6	348.6	348.6
	σ_{formal}	0.0	0.0	0.0	0.0
	σ_{data}	8.9	9.0	9.0	9.0
	T_max	383.1	399.3	382.0	378.8

1115

Code availability. The IDL and Python codes used to retrieve surface temperature and emissivity values are direct implementations of published methods. These scripts were developed independently by specific authors (FT, CR, FC) for internal research purposes, are not publicly released, and may be shared on a case-by-case basis upon justified request.

1120 *Data availability.* The MAJIS data acquired during the JUICE Moon–Earth flyby in August 2024 are currently under the mission’s cruise-phase proprietary period. These data will be made available through the ESA Planetary Science Archive following the first Cruise Archive Delivery, which is currently scheduled for six months after Earth Gravity Assist #3 in 2029. Diviner data are publicly accessible from the NASA Planetary Data System (PDS) Geosciences Node: <https://pds-geosciences.wustl.edu/missions/lro/diviner.htm>

Author contributions. FT, CR and FC carried out data analysis. FT prepared the manuscript with major contributions from CR and FC. TMP and BTG provided maps derived from Diviner data. FP, AM and FZ contributed to the discussion of results. FP and GP are respectively the PI and Co-PI of the MAJIS instrument. All authors have read and approved the manuscript.

1130 *Competing interests.* The authors declare that they have no conflict of interest.

Acknowledgements. The authors wish to thank ESA teams from SOC, MOC and ESTEC, as well as Airbus Defence and Space for their technical and operational support to the MAJIS project. JUICE is a mission under ESA leadership with contributions from its Member States, NASA, JAXA and the Israel Space Agency. It is the first Large-class mission in ESA's Cosmic Vision programme.

1135

Financial support. FT, GP, AM, CC and FZ acknowledge support from the Italian Space Agency (ASI), implementation agreement ASI-INAF n. 2023-6-HH.0. CR, FP, YL and CP acknowledge support from the Centre National d'Études Spatiales (CNES), contract CNES-CNRS n° 180 117.

1140 **References**

- Acton, C. H.: Ancillary data services of NASA's Navigation and Ancillary Information Facility, *Planet. Space Sci.*, 44(1), 65–70, [https://doi.org/10.1016/0032-0633\(95\)00107-7](https://doi.org/10.1016/0032-0633(95)00107-7), 1996.
- Acton, C. H., Bachman, N., Semenov, B., and Wright, E.: A look towards the future in the handling of space science mission geometry, *Planet. Space Sci.*, 150, 9–12, <https://doi.org/10.1016/j.pss.2017.02.013>, 2018.
- 1145 Adriani, A., Moriconi, M. L., Mura, A., Tosi, F., Sindoni, G., Noschese, R., Cicchetti, A., and Filacchione, G.: Juno's Earth flyby: the Jovian Infrared Auroral Mapper preliminary results, *Astrophys. Space Sci.*, 361(8), 272, <https://doi.org/10.1007/s10509-016-2842-9>, 2016.
- Adriani, A., Filacchione, G., Di Iorio, T., Turrini, D., Noschese, R., Cicchetti, A., Grassi, D., Mura, A., Sindoni, G., Zambelli, M., Piccioni, G., Capria, M. T., Tosi, F., Orosei, R., Dinelli, B. M., Moriconi, M. L., Roncon, E., Lunine, J. I., Becker, H. N., Bini, A., Barbis, A., Calamai, L., Pasqui, C., Nencioni, S., Rossi, M., Lastri, M., Formaro, R., and Olivieri, A.: JIRAM, the Jovian Infrared Auroral Mapper, *Space Sci. Rev.*, 213(1–4), 393–446, <https://doi.org/10.1007/s11214-014-0094-y>, 2017.
- 1150 Bandfield, J. L., Hayne, P. O., Williams, J.-P., Greenhagen, B. T., and Paige, D. A.: Lunar surface roughness derived from LRO Diviner Radiometer observations, *Icarus*, 248, 357–372, <https://doi.org/10.1016/j.icarus.2014.11.009>, 2015.
- 1155 Bandfield, J. L., Poston, M. J., Klima, R. L., and Edwards, C. S.: Widespread distribution of OH/H₂O on the lunar surface inferred from spectral data, *Nat. Geosci.*, 11(3), 173–177, <https://doi.org/10.1038/s41561-018-0065-0>, 2018.

- Bellucci, G., Brown, R. H., Formisano, V., Baines, K. H., Bibring, J.-P., Buratti, B. J., Capaccioni, F., Cerroni, P., Clark, R. N., Coradini, A., Cruikshank, D. P., Drossart, P., Jaumann, R., Langevin, Y., Matson, D. L., McCord, T. B., Mennella, V., Miller, E., Nelson, R. M., Nicholson, P. D., Sicardy, B., and Sotin, C.: Cassini/VIMS observations of the moon, *Adv. Space Res.*, 30(8), 1889–1894, [https://doi.org/10.1016/S0273-1177\(02\)00484-2](https://doi.org/10.1016/S0273-1177(02)00484-2), 2002.
- 1160 Brown, R. H., Baines, K. H., Bellucci, G., Bibring, J.-P., Buratti, B. J., Capaccioni, F., Cerroni, P., Clark, R. N., Coradini, A., Cruikshank, D. P., Drossart, P., Formisano, V., Jaumann, R., Langevin, Y., Matson, D. L., McCord, T. B., Mennella, V., Miller, E., Nelson, R. M., Nicholson, P. D., Sicardy, B., and Sotin, C.: The Cassini Visual And Infrared Mapping Spectrometer (VIMS) Investigation, *Space Sci. Rev.*, 115(1–4), 111–168, <https://doi.org/10.1007/s11214-004-1453-x>, 2004.
- 1165 Capria, M. T., Tosi, F., De Sanctis, M. C., Capaccioni, F., Ammannito, E., Frigeri, A., Zambon, F., Fonte, S., Palomba, E., Turrini, D., Titus, T. N., Schröder, S. E., Toplis, M., Li, J.-Y., Combe, J.-Ph., Raymond, C. A., and Russell, C. T.: Vesta surface thermal properties map, *Geophys. Res. Lett.*, 41(5), 1438–1443, <https://doi.org/10.1002/2013GL059026>, 2014.
- 1170 Chowdhury, A. R., Banerjee, A., Joshi, S. R., Dutta, M., Kumar, A., Bhattacharya, S., Amitabh, Rehman, S. U., Bhati, S., Karelia, J. C., Biswas, A., Saxena, A. R., Sharma, S., Somani, S. R., Bhagat, H. V., Sharma, J., Ghonia, D. N., Bokarwadia, B. B., and Parasar, A.: Imaging Infrared Spectrometer onboard Chandrayaan-2 Orbiter, *Curr. Sci.*, 118(3), 368–375, <https://doi.org/10.18520/cs/v118/i3/368-375>, 2020.
- Christensen, P. R., Hamilton, V. E., Anwar, S., Mehall, G., Spencer, J. R., Sunshine, J. M., and Levison, H. F.: Thermal Infrared Spectra of the Moon: Results From the Lucy Thermal Emission Spectrometer Observations, *J. Geophys. Res. Planets*, 130(5), e2024JE008493, <https://doi.org/10.1029/2024JE008493>, 2025.
- 1175 Davidsson, B. J. R. and Rickman, H.: Surface roughness and three-dimensional heat conduction in thermophysical models, *Icarus*, 243, 58–77, <https://doi.org/10.1016/j.icarus.2014.08.039>, 2014.
- Donaldson Hanna, K. L., Thomas, I. R., Bowles, N. E., Greenhagen, B. T., Pieters, C. M., Mustard, J. F., Jackson, C. R. M., and Wyatt, M. B.: Laboratory emissivity measurements of the plagioclase solid solution series under varying environmental conditions, *J. Geophys. Res.*, 117(E11), E11004, <https://doi.org/10.1029/2012JE004184>, 2012.
- 1180 Grasset, O., Dougherty, M. K., Coustenis, A., Bunce, E. J., Erd, C., Titov, D., Blanc, M., Coates, A., Drossart, P., Fletcher, L. N., Hussmann, H., Jaumann, R., Krupp, N., Lebreton, J.-P., Prieto-Ballesteros, O., Tortora, P., Tosi, F., and Van Hoolst, T.: JUPITER ICy moons Explorer (JUICE): An ESA mission to orbit Ganymede and to characterise the Jupiter system, *Planet. Space Sci.*, 78, 1–21, <https://doi.org/10.1016/j.pss.2012.12.002>, 2013.
- 1185 Greenhagen, B. T., Lucey, P. G., Wyatt, M. B., Glotch, T. D., Allen, C. C., Arnold, J. A., Bandfield, J. L., Bowles, N. E., Donaldson Hanna, K. L., Hayne, P. O., Song, E., Thomas, I. R., and Paige, D. A.: Global Silicate Mineralogy of the Moon from the Diviner Lunar Radiometer, *Science*, 329(5998), 1507–1509, <https://doi.org/10.1126/science.1192196>, 2010.

- 1190 Guerlet, S., Armante, R., Lauzanne, N., Poulet, F., Langevin, Y., Rodriguez, S., Fletcher, L., Fouchet, L., Piccioni, G., and Migliorini, A.: MAJIS performances in the infrared during the JUICE 2024 Earth fly-by: comparisons with IASI measurements and sensitivity to trace species, *Ann. Geophys.*, this issue, <https://doi.org/10.5194/egusphere-2026-805>, 2026.
- Haffoud, P., Poulet, F., Vincendon, M., Filacchione, G., Barbis, A., Guiot, P., Lecomte, B., Langevin, Y., Piccioni, G.,
1195 Dumesnil, C., Rodriguez, S., Carter, J., Stefani, S., Tommasi, L., Tosi, F., and Pilorget, C.: Calibration of MAJIS (Moons And Jupiter Imaging Spectrometer). III. Spectral calibration, *Rev. Sci. Instrum.*, 95(3), 031301, <https://doi.org/10.1063/5.0188944>, 2024.
- Hapke, B.: Bidirectional reflectance spectroscopy. I – Theory, *J. Geophys. Res.*, 86(B4), 3039–3054, <https://doi.org/10.1029/JB086iB04p03039>, 1981.
- 1200 Hapke, B.: Theory of Reflectance and Emittance Spectroscopy, Cambridge Univ. Press, New York, 2005.
- Keihm, S. J., Peters, K., Langseth, M. G., and Chute, J. L.: Apollo 15 measurement of lunar surface brightness temperatures: Thermal conductivity of the upper 1½ meters of regolith, *Earth Planet. Sci. Lett.*, 19(3), 337–351, [https://doi.org/10.1016/0012-821X\(73\)90084-8](https://doi.org/10.1016/0012-821X(73)90084-8), 1973.
- Keihm, S. J. and Langseth, M. G.: Lunar Microwave Brightness Temperature Observations Reevaluated in the Light of Apollo
1205 Program Findings, *Icarus*, 24(2), 211–230, [https://doi.org/10.1016/0019-1035\(75\)90100-1](https://doi.org/10.1016/0019-1035(75)90100-1), 1975.
- Keihm, S., Tosi, F., Kamp, L., Capaccioni, F., Gulkis, S., Grassi, D., Hofstadter, M., Filacchione, G., Lee, S., Giuppi, S., Janssen, M., and Capria, M. T.: Interpretation of combined infrared, submillimeter, and millimeter thermal flux data obtained during the Rosetta fly-by of Asteroid (21) Lutetia, *Icarus*, 221(1), 395–404, <https://doi.org/10.1016/j.icarus.2012.08.002>, 2012.
- 1210 Langevin, Y., Rodriguez, S., Guerlet, S., Poulet, F., Piccioni, G., Agostini, L., Armante, R., D’Aversa, E., Filacchione, G., Fletcher, L., Oliva, F., Royer, C., Seignovert, B., Stephan, K., Tosi, F., and Trent, T.: Post launch spectral and radiometric performances of MAJIS, the VIS-NIR imaging spectrometer of JUICE, *Ann. Geophys.*, this issue, doi: 10.5194/egusphere-2026-410, 2026.
- Li, S. and Li, L.: Radiative transfer modeling for quantifying lunar surface minerals, particle size, and submicroscopic metallic
1215 Fe, *J. Geophys. Res.*, 116(E9), E09001, <https://doi.org/10.1029/2011JE003837>, 2011.
- Li, S. and Milliken, R. E.: An empirical thermal correction model for Moon Mineralogy Mapper data constrained by laboratory spectra and Diviner temperatures, *J. Geophys. Res. Planets*, 121(10), 2081–2107, <https://doi.org/10.1002/2016JE005035>, 2016.
- Lommel, E. C. G.: “Die Photometrie der diffusen Zurückwerfung”, *Sitzungsber. d. math. phys. Class d. K. B. Acad. zu*
1220 *München*, 17, 95–132, 1887.
- Müller, T. G., Burgdorf, M., Ali-Lagoa, V., Buehler, S. A., and Prange, M.: The Moon at thermal infrared wavelengths: a benchmark for asteroid thermal models, *Astron. Astrophys.*, 650, A38, <https://doi.org/10.1051/0004-6361/202039946>, 2021.

- Mustard, J. F. and Hays, J. E.: Effects of hyperfine particles on reflectance spectra from 0.3 to 25 μm , *Icarus*, 125(1), 145–163, <https://doi.org/10.1006/icar.1996.5583>, 1997.
- Ojha, S. P., Dagar, A. K., Vikram, K. V. N. G., Bhattacharya, S., Bhattacharya, B. K., and Kiran Kumar, A. S.: Simultaneous physical retrieval of daytime lunar surface temperature and spectral emissivity in the 3–5 μm range from Chandrayaan-2 IIRS observations, *Curr. Sci.*, 126(7), 781–790, <https://doi.org/10.18520/cs/v126/i7/781-790>, 2024.
- Poulet, F., Piccioni, G., Langevin, Y., Dumesnil, C., Tommasi, L., Carlier, V., Filacchione, G., Amoroso, M., Arondel, A., D'Aversa, E., Barbis, A., Bini, A., Bolsée, D., Bousquet, P., Caprini, C., Carter, J., Dubois, J.-P., Condamin, M., Couturier, S., Dassas, K., Dexet, M., Fletcher, L., Grassi, D., Guerri, I., Haffoud, P., Larigauderie, C., Le Du, M., Mugnuolo, R., Pilato, G., Rossi, M., Stefani, S., Tosi, F., Vincendon, M., Zambelli, M., Arnold, G., Bibring, J.-P., Biondi, D., Boccaccini, A., Brunetto, R., Carapelle, A., Cisneros González, M., Hannou, C., Karatekin, O., Le Cle'ch, J.-C., Leyrat, C., Migliorini, A., Nathues, A., Rodriguez, S., Saggin, B., Sanchez-Lavega, A., Schmitt, B., Seignovert, B., Sordini, R., Stephan, K., Tobie, G., Zambon, F., Adriani, A., Altieri, F., Bockelée-Morvan, D., Capaccioni, F., De Angelis, S., De Sanctis, M.-C., Drossart, P., Fouchet, T., Gérard, J.-C., Grodent, D., Ignatiev, N., Irwin, P., Ligier, N., Manaud, N., Mangold, N., Mura, A., Pilorget, C., Quirico, E., Renotte, E., Strazzulla, G., Turrini, D., Vandaele, A.-C., Carli, C., Ciarniello, M., Guerlet, S., Lellouch, E., Mancarella, F., Morbidelli, A., Le Mouélic, S., Raponi, A., Sindoni, G., and Snels, M.: Moons and Jupiter Imaging Spectrometer (MAJIS) on Jupiter Icy Moons Explorer (JUICE), *Space Sci. Rev.*, 220(3), 27, <https://doi.org/10.1007/s11214-024-01057-2>, 2024.
- Poulet, F., Piccioni, G., Langevin, Y., Dumesnil, C., Carlier, V., Seignovert, B., Dexet, M., Fletcher, L. N., Leyrat, C., Altieri, F., Carter, J., D'Aversa, E., De Sanctis, M. C., Grassi, D., Guerlet, S., Le Mouélic, S., Migliorini, A., Oliva, F., Royer, C., Rodriguez, S., Stephan, K., Tosi, F., Zambon, F., Adriani, A., Arnold, G., Bibring, J.-P., Bockelée-Morvan, D., Brunetto, R., Capaccioni, F., Carli, C., Cavalié, T., Cisneros González, M., Ciarnello, M., De Angelis, M., Drossart, P., Filacchione, G., Fouchet, T., Gérard, J.-C., Grodent, D., Irwin, P., Jacquino, S., Karatekin, O., Lellouch, E., Ligier, N., Mangold, N., Mebsout, M., Merlin, F., Morbidelli, A., Mura, A., Nathues, A., Palumbo, M. E., Pilorget, C., Poch, O., Quirico, E., Raponi, A., Robert, S., Roussos, E., Sanchez-Lavega, A., Schmitt, B., Sindoni, G., Snels, M., Sordini, R., Stefani, S., Strazzulla, G., Trent, T., Tobie, G., Turrini, D., Vandaele, A.-C., Vincendon, M., Witasse, O., Vallat, C., and Moirano, A.: ESA/JUICE encounters Earth/Moon in 2024: Overview of the Moons And Jupiter Imaging Spectrometer (MAJIS) observations, *Ann. Geophys.*, this issue, <https://doi.org/10.5194/angeo-44-163-2026>, 2026.
- Paige, D. A., Foote, M. C., Greenhagen, B. T., Schofield, J. T., Calcutt, S., Vasavada, A. R., Preston, D. J., Taylor, F. W., Allen, C. C., Snook, K. J., Jakosky, B. M., Murray, B. C., Soderblom, L. A., Jau, B., Loring, S., Bulharowski, J., Bowles, N. E., Thomas, I. R., Sullivan, M. T., Avis, C., de Jong, E. M., Hartford, W., and McCleese, D. J.: The Lunar Reconnaissance Orbiter Diviner Lunar Radiometer Experiment, *Space Sci. Rev.*, 150(1–4), 125–160, <https://doi.org/10.1007/s11214-009-9529-2>, 2010.

- Ren, H., Nie, J., Dong, J., Liu, R., Fa, W., Hu, L., and Fan, W.: Lunar Surface Temperature and Emissivity Retrieval From Diviner Lunar Radiometer Experiment Sensor, *Earth Space Sci.*, 8(1), e01436, <https://doi.org/10.1029/2020EA001436>, 2021.
- 1260 Rodgers, C. D.: *Inverse Methods for Atmospheric Sounding – Theory and practice*, World Scientific Publishing Co., Singapore, Series on Atmospheric, Oceanic and Planetary Physics – Vol. 2, <https://doi.org/10.1142/3171>, ISBN: 978-981-02-2740-1, 2000.
- Royer, C., Haffoud, P., Langevin, Y., Poulet, F., Bockelée-Morvan, D., D’Aversa, E., Cisneros-González, M., Grassi, D., Ligier, N., Piccioni, G., Carter, J., Tosi, F., Vincendon, M., Zambon, F., Zakharov, V., Gilles, M., and Seignovert, B.:
 1265 A simulator of the MAJIS instrument onboard the JUICE mission: Description and application to operational and scientific cases, *Planet. Space Sci.*, 264, 106147, <https://doi.org/10.1016/j.pss.2025.106147>, 2025.
- Rozitis, B. and Green, S. F.: Directional characteristics of thermal-infrared beaming from atmosphereless planetary surfaces - a new thermophysical model, *Mon. Not. R. Astron. Soc.*, 415(3), 2042–2062, <https://doi.org/10.1111/j.1365-2966.2011.18718.x>, 2011.
- 1270 Rozitis, B., Emery, J. P., Siegler, M. A., Susorney, H. C. M., Molaro, J. L., Hergenrother, C. W., and Laretta, D. S.: Implications for Ice Stability and Particle Ejection From High-Resolution Temperature Modeling of Asteroid (101955) Benu, *J. Geophys. Res.*, 116, E09001, <https://doi.org/10.1029/2019JE006323>, 2020.
- Rubanenko, L., Schorghofer, N., Greenhagen, B. T., and Paige, D. A.: Equilibrium Temperatures and Directional Emissivity of Sunlit Airless Surfaces With Applications to the Moon, *J. Geophys. Res.*, 125(6),
 1275 <https://doi.org/10.1029/2020JE006377>, 2020.
- Seeliger, H.: Zur Theorie Beleuchtung der Grossen Planeten Insbesondere des Saturn, *Abhandl. Bayer. Akad. Wiss. Math. Naturw. Kl. II*, 16, 405–516, 1888.
- Salisbury, J. W., Walter, L. S. and Vergo, N: Mid-infrared (2.1–25 μm) reflectance spectra of powdered lunar soils and rock chips, U.S. Geological Survey, Open-File Report 87–263, <https://pubs.usgs.gov/of/1987/0263/report.pdf>, 1987.
- 1280 Salisbury, J. W., Basu, A., and Fischer, E. M.: Thermal Infrared Spectra of Lunar Soils, *Icarus*, 130(1), 125–139, <https://doi.org/10.1006/icar.1997.5809>, 1997.
- Seignovert, B., Poulet, F., Langevin, Y., D’Aversa, E., Ligier, N., Mesbout, M., Leyrat, C., Le Mouélic, S., Stephan, K., Palumbo, P., Agostini, L., Pensa, L., Le Deit, L., Cornet, T., Belgacem, I., Costa, M., and Escalante Lopez, A.: MAJIS onboard geometric calibration during the early cruise phase, *Ann. Geophys.*, in preparation, 2026.
- 1285 Shkuratov, Y., Kaydash, V., Korokhin, V., Velikodsky, Y., Opanasenko, N., and Videen, G.: Optical measurements of the Moon as a tool to study its surface, *Planet. Space Sci.*, 59(13), 1326–1371, <https://doi.org/10.1016/j.pss.2011.06.011>, 2011.
- Smith, D. E., Zuber, M. T., Neumann, G. A., Lemoine, F. G., Mazarico, E., Torrence, M., McGarry, J. F., Rowlands, D. D., Head, J. W., Duxbury, T. H., Aharonson, O., Lucey, P. G., Robinson, M. S., Barnouin, O. S., Cavanaugh, J. F., Sun,

- 1290 X., Liiva, P., Mao, D., Smith, J. C., and Bartels, A. E.: Initial observations from the Lunar Orbiter Laser Altimeter (LOLA), *Geophys. Res. Lett.*, 37(18), L18204, <https://doi.org/10.1029/2010GL043751>, 2010.
- Smith, D. E., Zuber, M. T., Neumann, G. A., Mazarico, E., Lemoine, F. G., Head, J. W., III, Lucey, P. G., Aharonson, O., Robinson, M., S., Sun, X., Torrence, M., H., Barker, M. K., Oberst, J., Duxbury, T. C., Mao, D. Barnouin, O. S., Jha, K., Rowlands, D. D., Goossens, S., Baker, D. Bauer, S., Gläser, P., Lemelin, M., Rosenburg, M., Sori, M. M., Whitten, 1295 J., and McLanahan, T.: Summary of the results from the lunar orbiter laser altimeter after seven years in lunar orbit, *Icarus*, 283, 70–91, <https://doi.org/10.1016/j.icarus.2016.06.006>, 2017.
- Spencer, J. R.: A rough-surface thermophysical model for airless planets, *Icarus*, 83(1), 27–38, [https://doi.org/10.1016/0019-1035\(90\)90004-S](https://doi.org/10.1016/0019-1035(90)90004-S), 1990.
- Speyerer, E. J., Robinson, M. S., Denevi, B. W., and LROC Science Team (2011). Lunar Reconnaissance Orbiter Camera 1300 global morphological map of the Moon, Paper presented at the 42nd Lunar Planetary Science Conference, Lunar and Planetary Science Institute, Houston, TX. <https://www.lpi.usra.edu/meetings/lpsc2011/pdf/2387.pdf>
- Tosi, F., Capria, M. T., De Sanctis, M. C., Combe, J.-Ph., Zambon, F., Nathues, A., Schröder, S. E., Li, J.-Y., Palomba, E., Longobardo, A., Blewett, D. T., Denevi, B. W., Palmer, E., Capaccioni, F., Ammannito, E., Titus, T. M., Mittlefehldt, D. W., Sunshine, J. M., Russell, C. T., and Raymond, C. A.: Thermal measurements of dark and bright surface features 1305 on Vesta as derived from Dawn/VIR, *Icarus*, 240, 36–57, <https://doi.org/10.1016/j.icarus.2014.03.017>, 2014.
- Tosi, F., Frigeri, A., Combe, J.-Ph., Zambon, F., De Sanctis, M. C., Ammannito, E., Longobardo, A., Hoffmann, M., Nathues, A., Garry, W. B., Blewett, D. T., Pieters, C. M., Palomba, E., Stephan, K., McFadden, L. A., McSween, H. Y., Russell, C. T., and Raymond, C. A.: Mineralogical analysis of the Oppia quadrangle of asteroid (4) Vesta: Evidence for 1310 occurrence of moderate-reflectance hydrated minerals, *Icarus*, 259, 129–149, <https://doi.org/10.1016/j.icarus.2015.05.018>, 2015.
- Tosi, F., Carrozzo, F. G., Raponi, A., De Sanctis, M. C., Thangjam, G., Zambon, F., Ciarniello, M., Nathues, A., Capria, M. T., Rognini, E., Ammannito, E., Hoffmann, M., Krohn, K., Longobardo, A., Palomba, E., Pieters, C. M., Stephan, K., Raymond, C. A., and Russell, C. T.: Mineralogy and temperature of crater Haulani on Ceres, *Meteorit. Planet. Sci.*, 53(9), 1902–1924, <https://doi.org/10.1111/maps.13078>, 2018.
- 1315 Tosi, F., Capaccioni, F., Capria, M. T., Mottola, S., Zinzi, A., Ciarniello, M., Filacchione, G., Hofstadter, M., Fonti, S., Formisano, M., Kappel, D., Kührt, E., Leyrat, C., Vincent, J.-B., Arnold, G., De Sanctis, M. C., Longobardo, A., Palomba, E., Raponi, A., Rousseau, B., Schmitt, B., Barucci, M. A., Bellucci, G., Benkhoff, J., Bockelée-Morvan, D., Cerroni, P., Combe, J.-Ph., Despan, D., Erard, S., Mancarella, F., McCord, T. B., Migliorini, A., Orofino, V., and Piccioni, G.: The changing temperature of the nucleus of comet 67P induced by morphological and seasonal effects, 1320 *Nat. Astron.*, 3(7), 649–658, <https://doi.org/10.1038/s41550-019-0740-0>, 2019.
- Tosi, F., Roatsch, T., Galli, A., Hauber, E., Lucchetti, A., Molyneux, P., Stephan, K., Achilleos, N., Bovolo, F., Carter, J., Cavalié, T., Cimò, G., D'Aversa, E., Gwinner, K., Hartogh, P., Huybrighs, H., Langevin, Y., Lellouch, E., Migliorini, A., Palumbo, P., Piccioni, G., Plaut, J. J., Postberg, F., Poulet, F., Retherford, K., Rezac, L., Roth, L., Solomonidou,

- 1325 A., Tobie, G., Tortora, P., Tubiana, C., Wagner, R., Wirström, E., Wurz, P., Zambon, F., Zannoni, M., Barabash, S., Bruzzone, L., Dougherty, M., Gladstone, R., Gurvits, L. I., Hussmann, H., Iess, L., Wahlund, J.-E., Witasse, O., Vallat, C., and Lorente, R.: Characterization of the Surfaces and Near-Surface Atmospheres of Ganymede, Europa and Callisto by JUICE, *Space Sci. Rev.*, 220(5), 59, <https://doi.org/10.1007/s11214-024-01089-8>, 2024.
- Vasavada, A. R., Paige, D. A., and Wood, S. E.: Near-Surface Temperatures on Mercury and the Moon and the Stability of Polar Ice Deposits, *Icarus*, 141(2), 179–193, <https://doi.org/10.1006/icar.1999.6175>, 1999.
- 1330 Vasavada, A. R., Bandfield, J. L., Greenhagen, B. T., Hayne, P. O., Siegler, M. A., Williams, J.-P., and Paige, D. A.: Lunar equatorial surface temperatures and regolith properties from the Diviner Lunar Radiometer Experiment, *J. Geophys. Res.*, 117(E12), E00H18, <https://doi.org/10.1029/2011JE003987>, 2012.
- Verma, P. A., Chauhan, M., and Chauhan, P.: Lunar surface temperature estimation and thermal emission correction using Chandrayaan-2 imaging infrared spectrometer data for H₂O & OH detection using 3 μ m hydration feature, *Icarus*, 383, <https://doi.org/10.1016/j.icarus.2022.115075>, 2022.
- 1335 Wagner, R. V., Speyerer, E. J., Robinson, M. S., and LROC Team (2015): New Mosaicked Data Products from the LROC Team, Paper presented at the 46th Lunar and Planetary Science Conference, Lunar and Planetary Institute, Houston, TX. <https://www.hou.usra.edu/meetings/lpsc2015/pdf/1473.pdf>
- Williams, J.-P., Paige, D. A., Greenhagen, B. T., and Sefton-Nash, E.: The global surface temperatures of the Moon as measured by the Diviner Lunar Radiometer Experiment, *Icarus*, 283, 300–325, <https://doi.org/10.1016/j.icarus.2016.08.012>, 2017.
- 1340 Williams, J.-P., Bandfield, J. L., Paige, D. A., Powell, T. M., Greenhagen, B. T., Taylor, S., Hayne, P. O., Speyerer, E. J., Ghent, R. R., and Costello, E. S.: Lunar cold spots and crater production on the Moon, *J. Geophys. Res. Planets*, 123(9), 2380–2392, <https://doi.org/10.1029/2018JE005652>, 2018.
- 1345 Wöhler, C., Grumpe, A., Berezhnoy, A. A., and Shevchenko, V. V.: Time-of-day–dependent global distribution of lunar surficial water/hydroxyl, *Sci. Adv.*, 3(9), <https://doi.org/10.1126/sciadv.1701286>, 2017.
- Wohlfarth, K., Wöhler, C., Hiesinger, H., and Helbert, J.: An advanced thermal roughness model for airless planetary bodies. Implications for global variations of lunar hydration and mineralogical mapping of Mercury with the MERTIS spectrometer, *Astron. Astrophys.*, 674, A69, <https://doi.org/10.1051/0004-6361/202245343>, 2023.
- 1350 Wu, Y., Meng, Z., Liu, Y., Huang, J., Zou, Y., Tang, X., Jiang, X., and Wang, Z.: Unveiling the secrets of the midinfrared (3.5 μ m) Moon: First global lunar image of a single exposure, *Geophys. Res. Lett.*, 48(4), e2020GL08883, <https://doi.org/10.1029/2020GL088393>, 2021.
- 1355 Zambon, F., Altieri, F., De Sanctis, M. C., Le Mouélic, S., Piccioni, G., Poulet, F., Langevin, Y., Royer, C., Tosi, F., Karatekin, O., Mura, A., and Carli, C.: Spectral analyzes of lunar regions observed by MAJIS during the JUICE Earth-Moon flyby, *Ann. Geophys.*, this issue, <https://doi.org/10.5194/egusphere-2026-876>, 2026.